Charged compact boson stars and shells in the presence of a cosmological constant

Sanjeev Kumar,[1,*] Usha Kulshreshtha,[2,3,†] and Daya Shankar Kulshreshtha[1,3,‡]

[1]*Department of Physics and Astrophysics, University of Delhi, Delhi-110007, India*
[2]*Department of Physics, Kirori Mal college, University of Delhi, Delhi-110007, India*
[3]*Department of Physics and Astronomy, Iowa State University, Ames, Iowa 50010, USA*

In this work, we study the boson stars and boson shells in a theory involving *massive* complex scalar fields coupled to the U(1) gauge field and gravity in a conical potential in the *presence* of a cosmological constant Λ which we treat as a free parameter taking positive and negative values and thereby allowing us to study the theory in the de Sitter and anti-de Sitter spaces respectively. Boson stars are found to come in two types, having either ball-like or shell-like charge density. We have studied the properties of these solutions and have also determined their domains of existence for some specific values of the parameters of the theory. Similar solutions have also been obtained by Kleihaus *et al.* in a theory involving *massless* complex scalar fields coupled to the U(1) gauge field and gravity in a conical potential in the *absence* of a cosmological constant Λ.

I. INTRODUCTION

Boson stars and boson shells representing the localized self-gravitating solutions were introduced long ago [1–3], and they have been studied very widely in the literature [4–28]. Such theories are being considered in the presence of positive [14–17] as well as negative [15,17–21] values of the cosmological constant Λ. The theories with positive values of Λ [corresponding to the de Sitter (dS) space] are relevant from the observational point of view as they describe a more realistic description of the compact stars in the Universe since all the observations seem to indicate the existence of a positive cosmological constant. Such theories are also being used to model the dark energy of the Universe. However, the theories with negative values of Λ [corresponding to the anti-de Sitter (AdS) space] are meaningful in the context of AdS/CFT correspondence [29–31].

In Ref. [16], we studied the boson stars and boson shells in a theory of complex scalar field coupled to the $U(1)$ gauge field A_μ and the gravity in the presence of a *positive* cosmological constant Λ (i.e. in the dS space), and in Ref. [15], we studied the *boson stars* in a theory of complex scalar field coupled to the $U(1)$ gauge field A_μ and the gravity in the presence of a positive as well as negative cosmological constant Λ, allowing us to study the theory in the dS as well as in the AdS space.

In the present work, we study not only the boson stars but also the boson shells in this theory of complex scalar field coupled to the $U(1)$ gauge field A_μ and the gravity and

a cosmological constant Λ, which we treat as a free parameter and which takes positive as well as negative values, thereby allowing us to study the theory in the dS as well as in the AdS space. As in Ref. [15], for our present investigations, also we study the theory in the presence of a potential: $V(|\Phi|) := (m^2|\Phi|^2 + \lambda|\Phi|)$ (with m and λ being constant parameters). We investigate the properties of the solutions of this theory and determine their domains of existence for some specific values of the parameters of the theory.

Similar solutions have also been obtained by Kleihaus *et al.* in a theory involving *massless* complex scalar fields coupled to the U(1) gauge field and gravity in a conical potential in the *absence* of a cosmological constant Λ [10,11]. They have obtained explicitly the domain of existence of compact boson stars and boson shells. They have also considered the boson shells, which do not have an empty inner region $r < r_i$, but instead they harbor a Schwarzschild black hole or a Reissner-Nordström black hole in the region $r < r_i$ [10,11]. Boson stars have also been studied in the presence of polynomial potentials [22–25].

In the present work, we construct the boson star and boson shell solutions of this theory numerically, and we study their properties, where we assume the interior of the shells to be empty space (dS-like or AdS-like). The action and the equations of motion are given in Sec. II. In Sec. III, the equations of motion are reexpressed in terms of the rescaled variables. The boundary conditions and the global charges are considered in Sec. IV. The numerical solutions for boson stars and boson shells are studied in Sec. V, and finally the summary and conclusions are given in Sec. VI.

[*]sanjeev.kumar.ka@gmail.com
[†]ushakulsh@gmail.com, ushakuls@iastate.edu
[‡]dskulsh@gmail.com, dayakuls@iastate.edu

II. ACTION, ANSÄTZE, AND EQUATIONS OF MOTION

The action of the theory under consideration reads

$$S = \int \left[\frac{R - 2\Lambda}{16\pi G} + \mathcal{L}_M \right] \sqrt{-g} d^4 x,$$

$$\mathcal{L}_M = -\frac{1}{4} F^{\mu\nu} F_{\mu\nu} - (D_\mu \Phi)^* (D^\mu \Phi) - V(|\Phi|),$$

$$D_\mu \Phi = (\partial_\mu \Phi + i e A_\mu \Phi), \qquad F_{\mu\nu} = (\partial_\mu A_\nu - \partial_\nu A_\mu). \quad (1)$$

Here, R is the Ricci curvature scalar, G is Newton's gravitational constant, and Λ is the cosmological constant. Also, $g = \det(g_{\mu\nu})$ where $g_{\mu\nu}$ is the metric tensor, and the asterisk in the above equation denotes complex conjugation. Using the variational principle, equations of motion are obtained as

$$G_{\mu\nu} \equiv R_{\mu\nu} - \frac{1}{2} g_{\mu\nu} R = 8\pi G T_{\mu\nu} - \Lambda g_{\mu\nu},$$

$$\partial_\mu(\sqrt{-g} F^{\mu\nu}) = -ie\sqrt{-g}[\Phi^*(D^\nu \Phi) - \Phi(D^\nu \Phi)^*],$$

$$D_\mu(\sqrt{-g} D^\mu \Phi) = 2m^2 \sqrt{-g} \Phi + \frac{\lambda}{2} \sqrt{-g} \frac{\Phi}{|\Phi|},$$

$$[D_\mu(\sqrt{-g} D^\mu \Phi)]^* = 2m^2 \sqrt{-g} \Phi^* + \frac{\lambda}{2} \sqrt{-g} \frac{\Phi^*}{|\Phi|}. \quad (2)$$

The energy-momentum tensor $T_{\mu\nu}$ is given by

$$T_{\mu\nu} = \left[\left(F_{\mu\alpha} F_{\nu\beta} g^{\alpha\beta} - \frac{1}{4} g_{\mu\nu} F_{\alpha\beta} F^{\alpha\beta} \right) \right.$$
$$+ (D_\mu \Phi)^* (D_\nu \Phi) + (D_\mu \Phi)(D_\nu \Phi)^*$$
$$\left. - g_{\mu\nu}((D_\alpha \Phi)^*(D_\beta \Phi))g^{\alpha\beta} - g_{\mu\nu} V(|\Phi|) \right]. \quad (3)$$

To construct spherically symmetric solutions, we adopt a static spherically symmetric metric with Schwarzschild-like coordinates [10,11]:

$$ds^2 = [-A^2 N dt^2 + N^{-1} dr^2 + r^2(d\theta^2 + \sin^2\theta d\varphi^2)]. \quad (4)$$

This leads to the components of the Einstein tensor ($G_{\mu\nu}$),

$$G_t^t = \left[\frac{-[r(1-N)]'}{r^2} \right], \qquad G_r^r = \left[\frac{2rA'N - A[r(1-N)]'}{Ar^2} \right],$$

$$G_\theta^\theta = \left[\frac{2r[rA'N]' + [Ar^2N']'}{2Ar^2} \right] = G_\varphi^\varphi. \quad (5)$$

Here, the arguments of the functions $A(r)$ and $N(r)$ have been suppressed. For solutions with vanishing magnetic field, the Ansätze for the matter fields have the form [10,11]

$$\Phi(x^\mu) = \phi(r)e^{i\omega t}, \qquad A_\mu(x^\mu)dx^\mu = A_t(r)dt. \quad (6)$$

With these Ansätze, the Einstein equations

$$G_t^t = 8\pi G T_t^t - \Lambda, \qquad G_r^r = 8\pi G T_r^r - \Lambda,$$
$$G_\theta^\theta = 8\pi G T_\theta^\theta - \Lambda, \qquad G_\varphi^\varphi = 8\pi G T_\varphi^\varphi - \Lambda \quad (7)$$

with the arguments of $A(r)$, $N(r)$, $\phi(r)$, and $A_t(r)$ being suppressed, reduce to

$$\frac{-1}{r^2}[r(1-N)]' = \frac{-8\pi G}{2A^2 N e^2} \left\{ N[(\omega + eA_t)']^2 + (\omega + eA_t)^2(\sqrt{2}e\phi)^2, \right.$$
$$\left. + A^2 N^2(\sqrt{2}e\phi')^2 + A^2 N \left[m^2(\sqrt{2}e\phi)^2 + \frac{2e\lambda}{\sqrt{2}}(\sqrt{2}e\phi) \right] \right\} - \Lambda \quad (8)$$

$$\frac{2rA'N - A[r(1-N)]'}{Ar^2} = \frac{8\pi G}{2A^2 N e^2} \left\{ -N[(\omega + eA_t)']^2 + (\omega + eA_t)^2(\sqrt{2}e\phi)^2, \right.$$
$$\left. + A^2 N^2(\sqrt{2}e\phi')^2 - A^2 N \left[m^2(\sqrt{2}e\phi)^2 + \frac{2e\lambda}{\sqrt{2}}(\sqrt{2}e\phi) \right] \right\} - \Lambda \quad (9)$$

$$\frac{2r[rA'N]' + [Ar^2N']'}{2Ar^2} = \frac{8\pi G}{2A^2 N e^2} \left\{ N[(\omega + eA_t)']^2 + (\omega + eA_t)^2(\sqrt{2}e\phi)^2, \right.$$
$$\left. - A^2 N^2(\sqrt{2}e\phi')^2 - A^2 N \left[m^2(\sqrt{2}e\phi)^2 + \frac{2e\lambda}{\sqrt{2}}(\sqrt{2}e\phi) \right] \right\} - \Lambda. \quad (10)$$

Here, the prime denotes differentiation with respect to r, and the equation $G^\varphi_\varphi = 8\pi G T^\varphi_\varphi - \Lambda$ also leads to an equation identical with Eq. (10).

III. EQUATIONS OF MOTION IN TERMS OF RESCALED VARIABLES

We redefine $\phi(r)$ and $A_t(r)$ as

$$h(r) = \frac{\sqrt{2}e\phi(r)}{m}, \qquad b(r) = \frac{\omega + eA_t(r)}{m}. \qquad (11)$$

We introduce new dimensionless constant parameters:

$$\alpha = \frac{4\pi G m^2}{e^2}, \qquad \tilde{\lambda} = \frac{\lambda e}{\sqrt{2}m^3}, \qquad \tilde{\Lambda} = \frac{\Lambda}{m^2}. \qquad (12)$$

Introducing a dimensionless coordinate $\hat{r}$ defined by $\hat{r} = mr$ (implying $\frac{d}{dr} = m\frac{d}{d\hat{r}}$), Eq. (11) reads as

$$h(\hat{r}) = \frac{\sqrt{2}e\phi(\hat{r})}{m}, \qquad b(\hat{r}) = \frac{\omega + eA_t(\hat{r})}{m}. \qquad (13)$$

Equations of motion in terms of $h(\hat{r})$ and $b(\hat{r})$ [where the primes denote differentiation with respect to $\hat{r}$] read

$$(AN\hat{r}^2 h')' = \frac{\hat{r}^2}{AN}[A^2N(h + \tilde{\lambda}\text{sign}(h)) - b^2 h], \qquad (14)$$

$$\left[\frac{\hat{r}^2 b'}{A}\right]' = \left[\frac{\hat{r}^2 h^2 b}{AN}\right], \qquad (15)$$

where

$$\text{sign}(h) = \begin{cases} \pm 1 & h > 0, \ h < 0 \\ 0 & h = 0. \end{cases}$$

With the above Ansätze (with the primes denoting the differentiation with respect to $\hat{r}$), we obtain

$$\frac{1}{\hat{r}^2}[\hat{r}(1-N)]' = \left[\tilde{\Lambda} + \frac{\alpha}{A^2N}(b^2 h^2 + Nb'^2 + A^2N^2 h'^2 + A^2N(h^2 + 2\tilde{\lambda}h))\right], \qquad (16a)$$

$$\frac{2\hat{r}A'N - A[\hat{r}(1-N)]'}{A\hat{r}^2} = \left[-\tilde{\Lambda} + \frac{\alpha}{A^2N}(b^2 h^2 - Nb'^2 + A^2N^2 h'^2 - A^2N(h^2 + 2\tilde{\lambda}h))\right), \qquad (16b)$$

$$\frac{2r[rA'N]' + [Ar^2N']'}{2Ar^2} = \left[-\tilde{\Lambda} + \frac{\alpha}{A^2N}(b^2 h^2 + Nb'^2 - A^2N^2 h'^2 - A^2N(h^2 + 2\tilde{\lambda}h))\right], \qquad (16c)$$

$$h'' = \left[\frac{A^2N(h + \tilde{\lambda}\text{sign}(h)) - b^2 h}{A^2N^2} - \frac{2h'}{\hat{r}} - h'\left(\frac{A'}{A}\frac{N'}{N}\right)\right], \qquad (16d)$$

$$b'' = \left[\frac{bh^2}{N} + \frac{b'A'}{A} - \frac{2b'}{\hat{r}}\right]. \qquad (16e)$$

Simplifying Eqs. (16a) and (16b) for A' and N' and also using Eqs. (16d) and (16e), we get

$$h'' = \left[\frac{\alpha\hat{r}h'}{A^2N}(A^2 h^2 + 2A^2 h\tilde{\lambda} + b'^2) - \frac{h'(1 + N - \tilde{\Lambda}\hat{r}^2)}{\hat{r}N}\right.$$

$$\left. + \frac{A^2Nh + A^2N\tilde{\lambda}\text{sign}(h) - b^2 h}{A^2N^2}\right], \qquad (17a)$$

$$b'' = \left[\frac{\alpha}{A^2N^2}\hat{r}b'(A^2N^2 h'^2 + b^2 h^2) - \frac{2b'}{\hat{r}} + \frac{bh^2}{N}\right], \qquad (17b)$$

$$N' = \left[\frac{1 - N - \tilde{\Lambda}\hat{r}^2}{\hat{r}} - \frac{\alpha\hat{r}}{A^2N}(A^2N^2 h'^2 + Nb'^2 + b^2 h^2\right.$$

$$\left. + A^2Nh^2 + 2A^2Nh\tilde{\lambda})\right], \qquad (17c)$$

$$A' = \left[\frac{\alpha\hat{r}}{AN^2}(A^2N^2 h'^2 + b^2 h^2)\right]. \qquad (17d)$$

To solve Eqs. (17a), (17b), (17c), and (17d) numerically, we introduce a new coordinate x as follows [10,11],

$$\hat{r} = \hat{r}_i + x(\hat{r}_o - \hat{r}_i), \qquad 0 \le x \le 1, \qquad (18)$$

implying that $\hat{r} = \hat{r}_i$ at $x = 0$ and $\hat{r} = \hat{r}_o$ at $x = 1$. Thus, the inner and outer boundaries of the shell are always at $x = 0$ and $x = 1$ respectively, while their radii $\hat{r}_i$ and $\hat{r}_o$ become free parameters.

IV. BOUNDARY CONDITIONS AND GLOBAL CHARGES

For the metric function $A(r)$, we choose the boundary condition

$$A(\hat{r}_o) = 1, \tag{19}$$

where r_o is the outer radius of the shell. For constructing globally regular ball-like boson star solutions, we choose

$$N(0) = 1, \qquad b'(0) = 0, \qquad h'(0) = 0,$$
$$h(\hat{r}_o) = 0, \qquad h'(\hat{r}_o) = 0. \tag{20}$$

For the boson stars, for the positive $\tilde{\Lambda}$, we match the exterior region $\hat{r} > \hat{r}_o$ with the Reissner-Nordström de Sitter solutions, and for the negative $\tilde{\Lambda}$, we match with the Reissner-Nodrstroöm anti-de Sitter solutions.

For globally regular boson shell solutions with empty space-time in the interior of the shells, $r < r_i$, we choose the boundary conditions

$$N(\hat{r}_i) = 1 - \frac{\Lambda}{3}\hat{r}_i^2, \qquad b'(\hat{r}_i) = 0, \qquad h(\hat{r}_i) = 0,$$
$$h'(\hat{r}_i) = 0, \qquad h(\hat{r}_o) = 0, \qquad h'(\hat{r}_o) = 0, \tag{21}$$

where $\hat{r}_i$ and $\hat{r}_o$ are the inner and outer radii of the shell.

For the boson shells, for the positive $\tilde{\Lambda}$, we match the interior region $\hat{r} < \hat{r}_i$ with the de Sitter vacuum solution and the exterior region $\hat{r} > \hat{r}_o$ with the Reissner-Nordström de Sitter solutions. However, for the negative $\tilde{\Lambda}$, we match the interior region $\hat{r} < \hat{r}_i$ with the anti-de Sitter vacuum solution and the exterior region $\hat{r} > \hat{r}_o$ with the Reissner-Nordström anti-de Sitter solutions.

The conserved Noether current is given by

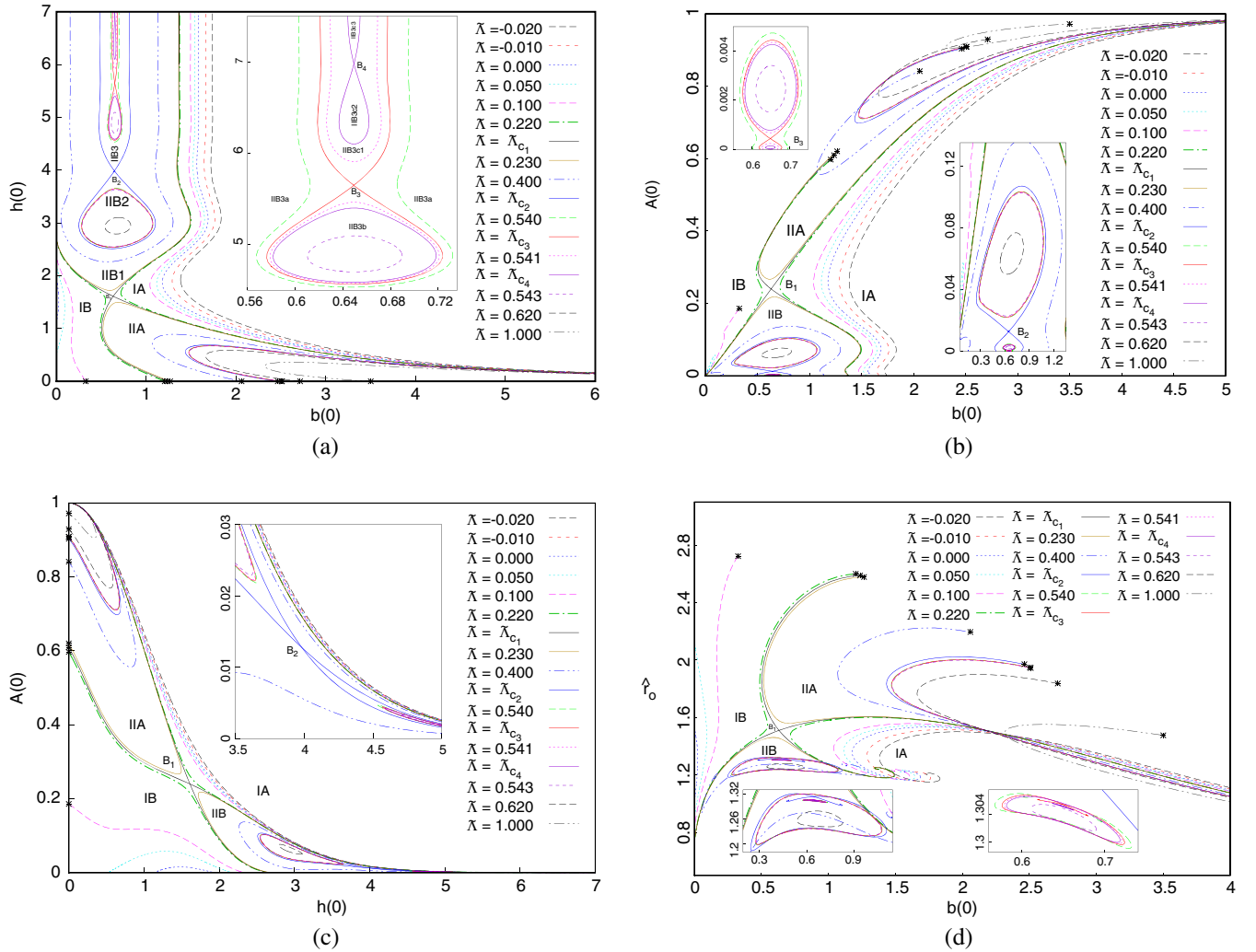$$j^\mu = -ie\{\Phi(D^\mu\Phi)^* - \Phi^*(D^\mu\Phi)\}, \qquad D_\mu j^\mu = 0. \tag{22}$$

FIG. 1.   Figures (a) to (c) depict the phase diagrams of the theory showing respectively the plots of $h(0)$ vs $b(0)$, $A(0)$ vs $b(0)$, and $A(0)$ vs $h(0)$ [where $h(0)$, $b(0)$, and $A(0)$ denote the values of these fields at the center of the star], and Fig. (d) depicts a plot of $\hat{r}_o$ vs $b(0)$. Also, all these four figures show the plots for different values of $\tilde{\Lambda}$ ranging from $\tilde{\Lambda} = -0.020$ to $\tilde{\Lambda} = +1.000$ (covering the AdS as well as dS spaces). The figures shown in the insets in Figs. (a)–(d) represent particular sections of these figures with better precision.

The charge Q_{sh} of a boson shell is given by

$$Q_{sh} = -\frac{1}{4\pi}\int_{\hat{r}_i}^{\hat{r}_0} j^t\sqrt{-g}d\hat{r}d\theta d\phi, \qquad j^t = -\frac{h^2 b}{A^2 N}.$$

For a boson star, the integration interval starts from zero.

For all the gravitating solutions, we obtain the mass parameter M (in the units employed):

$$M = \left(1 - N(\hat{r}_o) + \frac{\alpha Q^2}{\hat{r}_o^2} - \frac{\Lambda}{3}\hat{r}_o^2\right)\frac{\hat{r}_o}{2}. \qquad (23)$$

V. NUMERICAL SOLUTIONS FOR BOSON STARS AND BOSON SHELLS

In this section, we consider the numerical solutions for the boson stars and boson shells for the positive values of $\tilde{\Lambda}$ (corresponding to the dS space) as well as for the negative values of $\tilde{\Lambda}$ (corresponding to the AdS space).

For the present work, we study the numerical solutions of Eqs. (17a), (17b), (17c), and (17d) [by introducing a coordinate x defined by Eq. (18)] under the boundary conditions given by Eqs. (19) and (20) for boson stars and under Eqs. (19) and (20) for boson shells, and we determine their domain of existence for some specific values of the parameters of the theory. We wish to mention that for our numerical investigations we have used the well-known Newton-Raphson scheme with the adaptive step-size Runge-Kutta method of order 4.

Our theory has three parameters, α, $\tilde{\lambda}$, and $\tilde{\Lambda}$, and we study the theory by keeping α and $\tilde{\lambda}$ fixed (namely $\alpha = 0.2$ and $\tilde{\lambda} = 1.0$), and we study the theory of boson stars and boson shells for different values of $\tilde{\Lambda}$ giving it
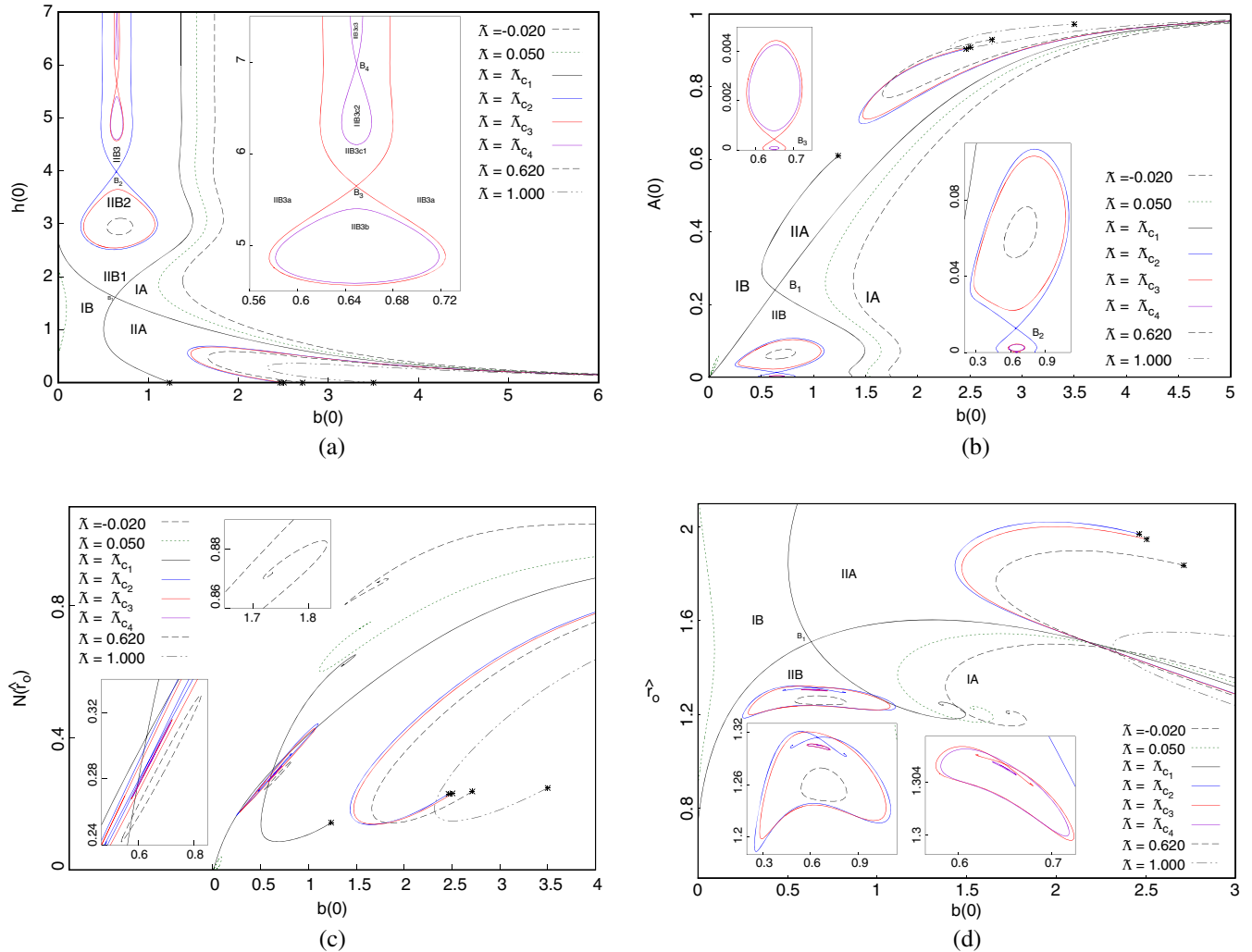

FIG. 2. Figures (a) and (b) depict the phase diagrams of the theory showing respectively the plots of $h(0)$ vs $b(0)$ and $A(0)$ vs $b(0)$ [where $h(0)$, $b(0)$, and $A(0)$ denote the values of these fields at the center of the star]. Figure (c) depicts the phase diagram of the theory involving $N(\hat{r}_o)$ and $b(0)$ [where $N(\hat{r}_o)$ denotes the value of the field at the outer radius of the star], and Fig. (d) depicts a plot of $\hat{r}_o$ vs $b(0)$. Also, all these four figures show the plots for different values of $\tilde{\Lambda}$ ranging from $\tilde{\Lambda} = -0.020$ to $\tilde{\Lambda} = +1.000$ (covering the AdS as well as dS spaces). The figures shown in the insets in Figs. (a)–(d) represent particular sections of these figures with better precision.
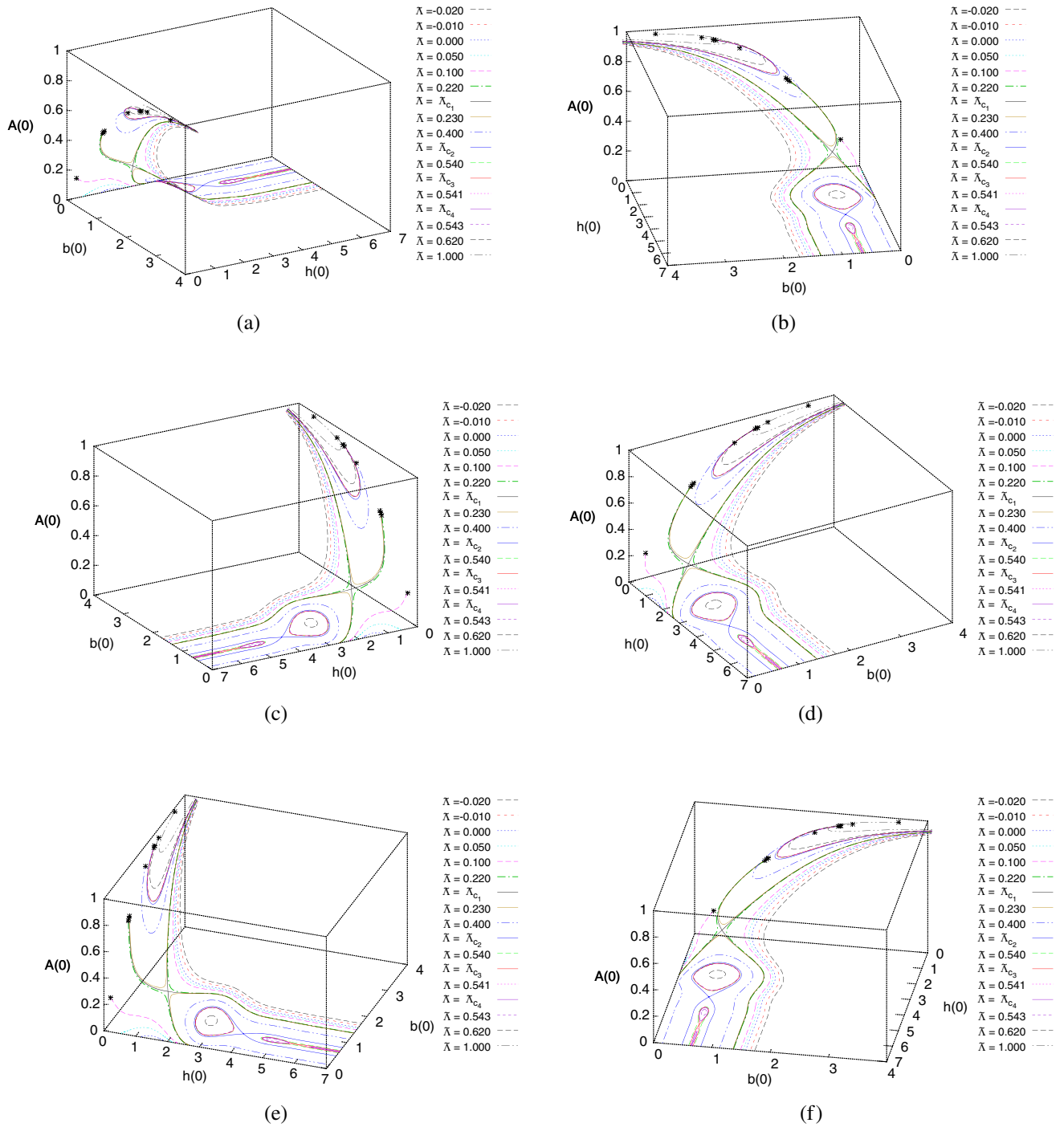
(a)

(b)

(c)

(d)

(e)

(f)

FIG. 3.   Properties of gravitating boson stars: Figs. (a), (b), (c), (d), (e), and (f) show the 3D plot (with six different viewing angles) of the scalar field h and the U(1) gauge field b vs the metric field A at the center of the boson star for several values of the cosmological constant $\tilde{\Lambda}$. For the viewing angles denoted by (θ, ϕ), we use the convention such that θ denotes the angle of rotation about the ox axis in the anticlockwise direction, and it can take values between 0 to π, and ϕ is the angle of rotation along the oz' axis also in the anticlockwise direction, and it can take values between 0 to 2π. Figures (a)–(f) correspond respectively to the values $(\theta, \phi) \equiv (60, 60)$, (60,170), (60,240), (130,30), (130,70), and (130,350).

positive as well as negative values, and we discuss the corresponding physics. In the first place, we discuss in details our results for the case of boson stars. For this, we study and discuss the phase diagrams of our theory

for boson stars as shown in Figs 1(a), 1(b), and 1(c). In Fig. 1(a), we study it for the fields $h(0)$ and $b(0)$; in Fig. 1(b), we study it for the fields $A(0)$ and $b(0)$; and in Fig. 1(c), we study it for the fields $A(0)$ and $h(0)$

[where $h(0)$, $b(0)$, and $A(0)$ denote the values of these fields at the center of the star]. Figure 1(d) depicts the plot of $\hat{r}_o$ vs $b(0)$ for different values of $\tilde{\Lambda}$ ranging from $\tilde{\Lambda} = -0.020$ to $\tilde{\Lambda} = +1.000$ (covering the AdS as well as dS spaces). Also, the figures shown in the

insets in Fig. 1(a)–1(d) represent particular sections of these figures with better precision. The asterisks shown in Figs. 1(a)–1(d) corresponding to $h(0) = 0$ represent the transition points from the boson stars to the boson shells.
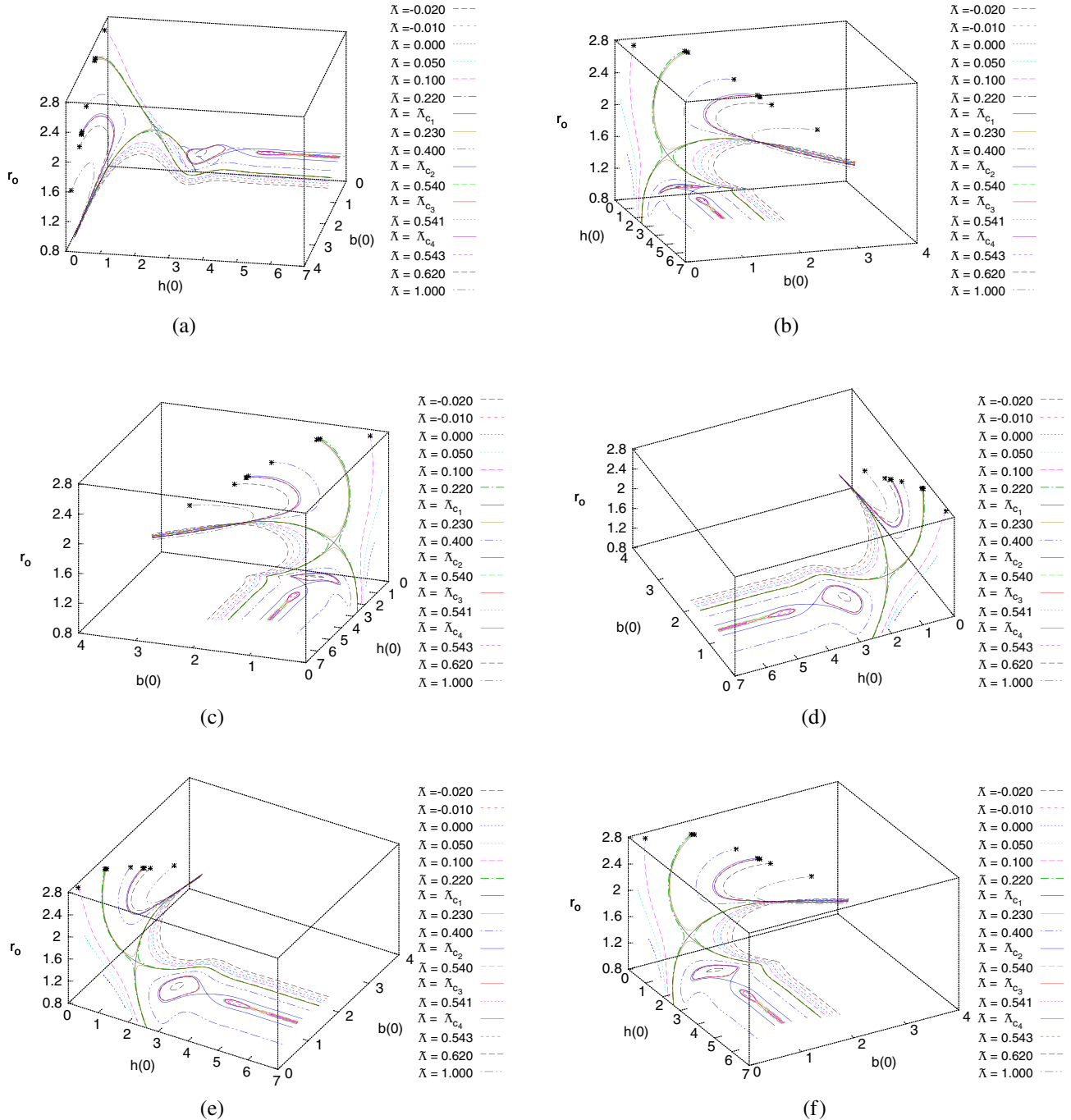

FIG. 4.   Properties of gravitating boson stars: Figs. (a), (b), (c), (d), (e), and (f) show the 3D plot [with six different viewing angles) of the scalar field h and the U(1) gauge field b at the center of the boson star vs the radius of the star $\hat{r}_o$ for several values of the cosmological constant $\tilde{\Lambda}$]. For the viewing angles denoted by (θ, ϕ), we use the convention such that θ denotes the angle of rotation about the ox axis in the counterclockwise direction, and it can take values between zero and π, and ϕ is the angle of rotation along the oz' axis also in the counterclockwise direction, and it can take values between 0 to 2π. Figures (a)–(f) correspond respectively to the values $(\theta, \phi) \equiv (60, 100)$, (112,17), (60,200), (35,245), (140,60), and (130,30).

The phase diagram of the theory involving the fields $N(\hat{r}_o)$ and $b(0)$ is shown in Fig. 2(c) [where $N(\hat{r}_o)$ denotes the value of the field at the outer radius of the star and $b(0)$ denotes the value of the gauge field at the center of the boson star] for different values of $\tilde{\Lambda}$ ranging from $\tilde{\Lambda} = -0.020$ to $\tilde{\Lambda} = +1.000$ (covering the AdS as well as dS spaces).

Our present studies involve investigations corresponding to several properties of the boson stars and boson shells as explained in details in this section. In the case of boson stars, we study not only the phase diagrams of the theory for the scalar vs vector fields at the center of the star (as studied in the work of Ref. [15]) but also the phase diagrams of this theory for (i) the case of the metric field $A(\hat{r})$ at the center of the boson star [i.e. $A(0)$] vs the vector field $b(\hat{r})$ at the center of the star [i.e. $b(0)$] [depicted in Fig 1(b)]; for (ii) the case of the metric field $A(\hat{r})$ at the center of the boson star [i.e. $A(0)$] vs the scalar field $h(\hat{r})$ at the center of the star [i.e. $h(0)$] [depicted in Fig 1(c)]; and for (iii) the case of the phase diagram of the theory

involving the metric field $N(\hat{r})$ at the outer radius of the boson star [i.e. $N(\hat{r}_o)$] vs $b(0)$ [depicted in Fig 2(c)]. Also, all these studies are done for different values of $\tilde{\Lambda}$ ranging from $\tilde{\Lambda} = -0.020$ to $\tilde{\Lambda} = +1.000$ covering the AdS and dS spaces.

As discussed in details in Ref. [15], some interesting phenomena occur hear near some specific values of $\tilde{\Lambda}$ when the system is seen to have four bifurcation points B_1, B_2, B_3, and B_4 which correspond to four different values of the cosmological constant $\tilde{\Lambda}$: $\tilde{\Lambda}_{c_1} \simeq 0.22521$, $\tilde{\Lambda}_{c_2} \simeq 0.52605$, $\tilde{\Lambda}_{c_3} \simeq 0.54076$, and $\tilde{\Lambda}_{c_4} \simeq 0.541250$ respectively. The theory is seen to have rich physics in the domain $\tilde{\Lambda} = +0.500$ to $\tilde{\Lambda} \simeq +0.62$.

For a proper understanding of the richness of the physics observed in our phase diagrams obtained in the present investigations, it is important to recapitulate some of the related important points from our earlier investigation (cf. the work of Ref. [15]). In fact, an understanding of the physics contents of the phase diagrams depicted in
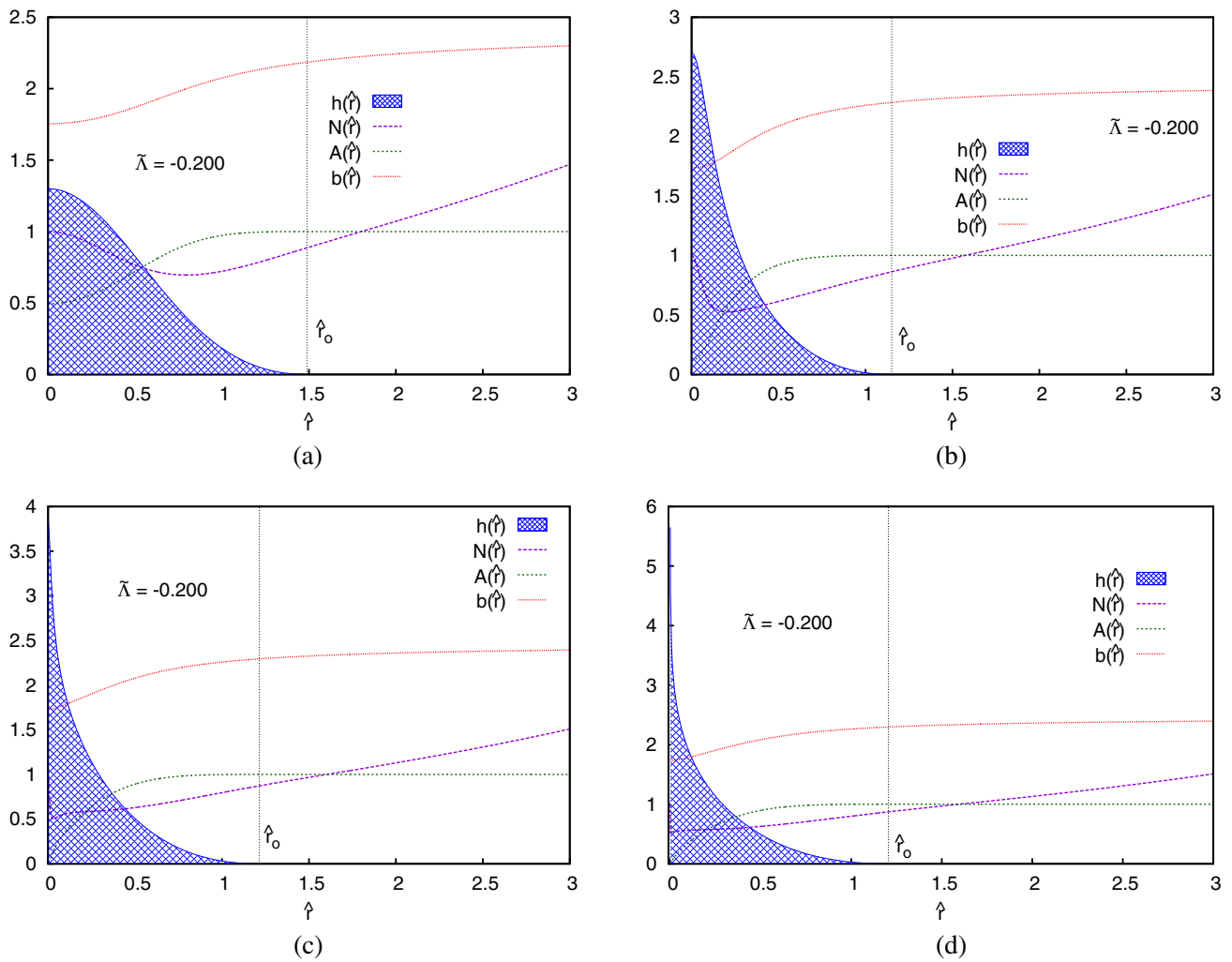

FIG. 5. Figures (a)–(d) depict plots of $h(\hat{r})$, $N(\hat{r})$, $A(\hat{r})$, and $b(\hat{r})$ vs $\hat{r}$ for $\tilde{\Lambda} = -0.200$ (which corresponds to the AdS space).
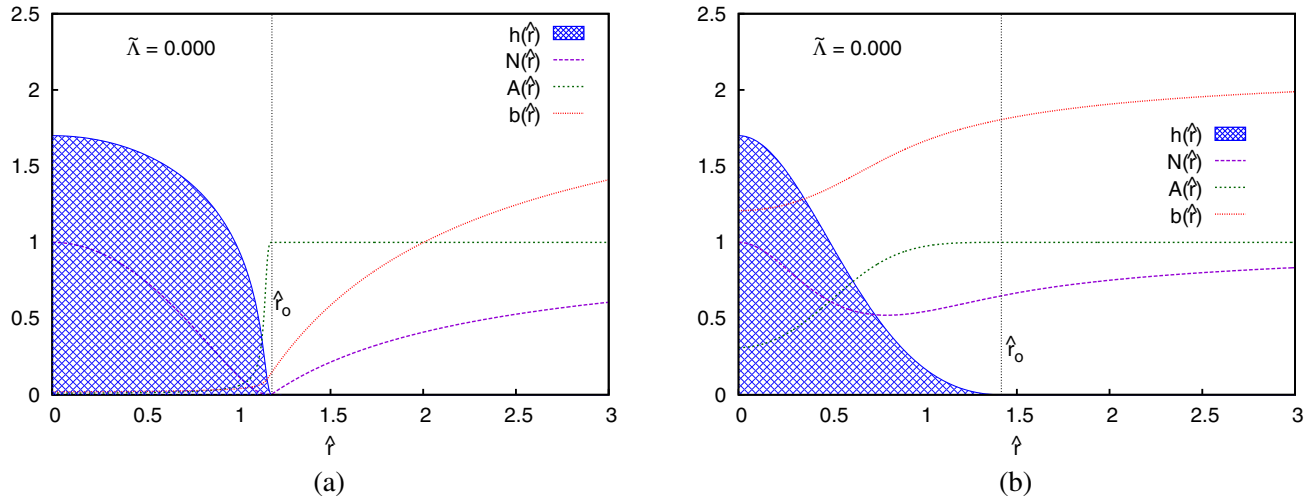
FIG. 6. Figures (a) and (b) depict plots of $h(\hat{r})$, $N(\hat{r})$, $A(\hat{r})$, and $b(\hat{r})$ vs $\hat{r}$ for $\tilde{\Lambda} = 0.000$.
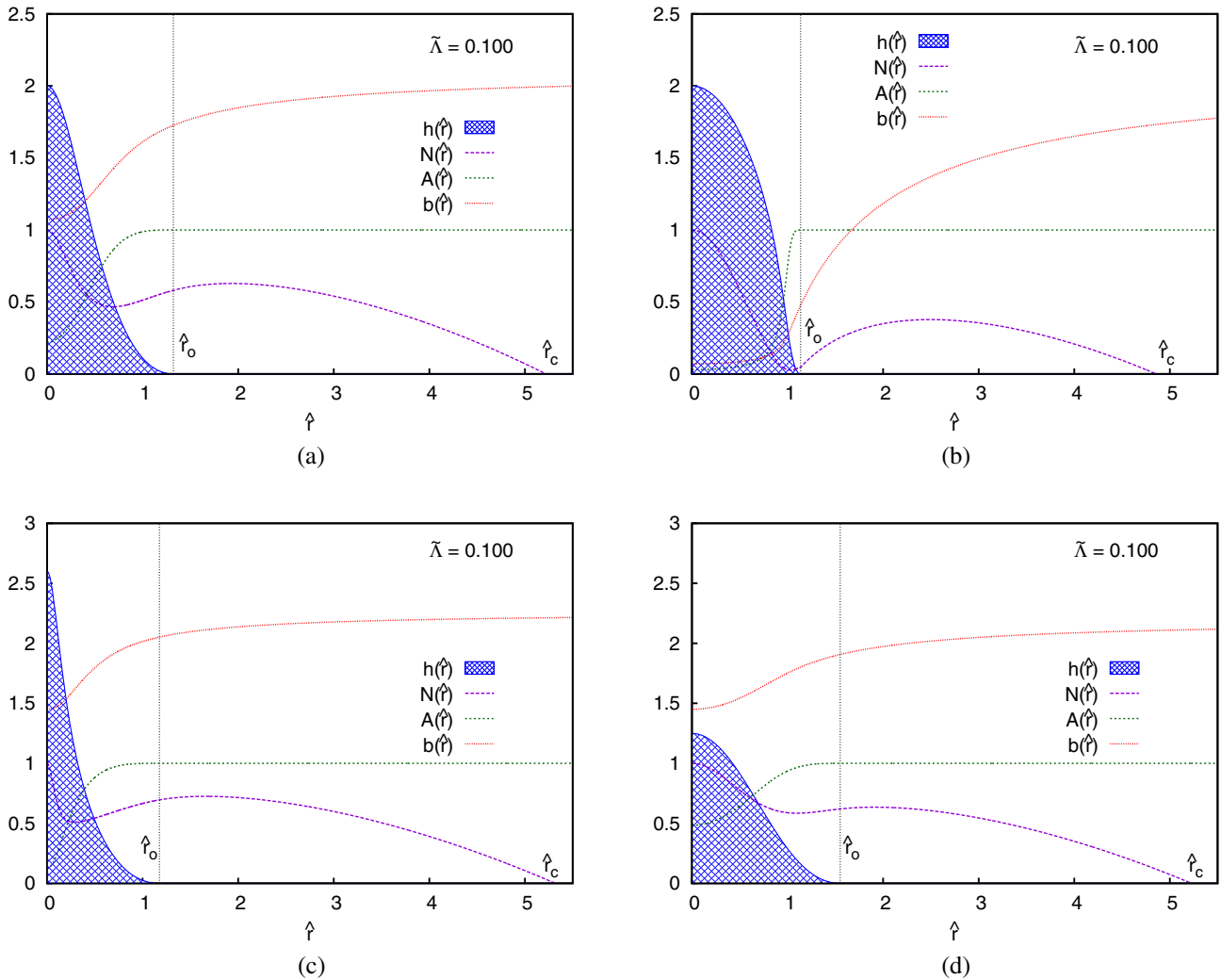

FIG. 7. Figures (a) to (d) depict plots of $h(\hat{r})$, $N(\hat{r})$, $A(\hat{r})$, and $b(\hat{r})$ vs $\hat{r}$ for $\tilde{\Lambda} = 0.100$ (which corresponds to the dS space).

Figs. 1(b) and 1(c) necessitates a proper recount of the physics contents of the phase diagram depicted in Fig. 1(a).

In Fig. 1(a), we have divided our phase diagram into four regions denoted by IA, IB, IIA, and IIB in the vicinity of B_1. The asterisks seen in Fig. 1(a) coinciding with the axis $b(0)$ [i.e. corresponding to $h(0) = 0$] represent the transition points from the boson stars to boson shells.

The regions IA, IB, and IIA do not have any bifurcation points; however, the region IIB is seen to contain rich physics evidenced by the occurrence of more bifurcation points in this region. For better details, region IIB is also plotted in Fig. 1(b). Region IIB is further divided into regions IIB1, IIB2, and IIB3 in the vicinity of B_2 as seen in Fig. 1(a).

Region IIB3 is seen to have further bifurcation point B_3. In the vicinity of B_3, we further subdivide the phase diagram into regions IIB3a, IIB3b, and IIB3c. Region IIB3b is seen to have closed loops, and the behavior of the phase diagram in this region is akin to that of region IIB2. Also, the figures shown in the inset represent part of the diagrams with better precision.

Region IIB3c is again seen to have a further bifurcation point B_4, and in the vicinity of B_4, we again subdivide the phase diagram in to regions IIB3c1, IIB3c2, and IIB3c3. Region IIB3c2 is again seen to have closed loops, and the behavior of the phase diagram in this region is akin to that of regions IIB2 and IIB3b.

Regions IA and IB could be divided into two subregions corresponding to positive and negative values of $\tilde{\Lambda}$, implying the dS and AdS regions corresponding to positive and negative values of $\tilde{\Lambda}$. In region IA, as we change the value of $\tilde{\Lambda}$ in the AdS region from $\tilde{\Lambda} = 0.000$ to $\tilde{\Lambda} = -0.020$, we observe a continuous deformation of the curves in the phase diagram. In region IB, as we change the value of $\tilde{\Lambda}$ in the domain $\tilde{\Lambda} = 0.000$ to $\tilde{\Lambda} \simeq -0.02$, the theory is seen to have solutions for the boson stars only, without having transition points from boson stars to boson shells, and the curves corresponding to the solutions disappear in the phase diagram of the theory for the values $\tilde{\Lambda} \lesssim -0.02$.
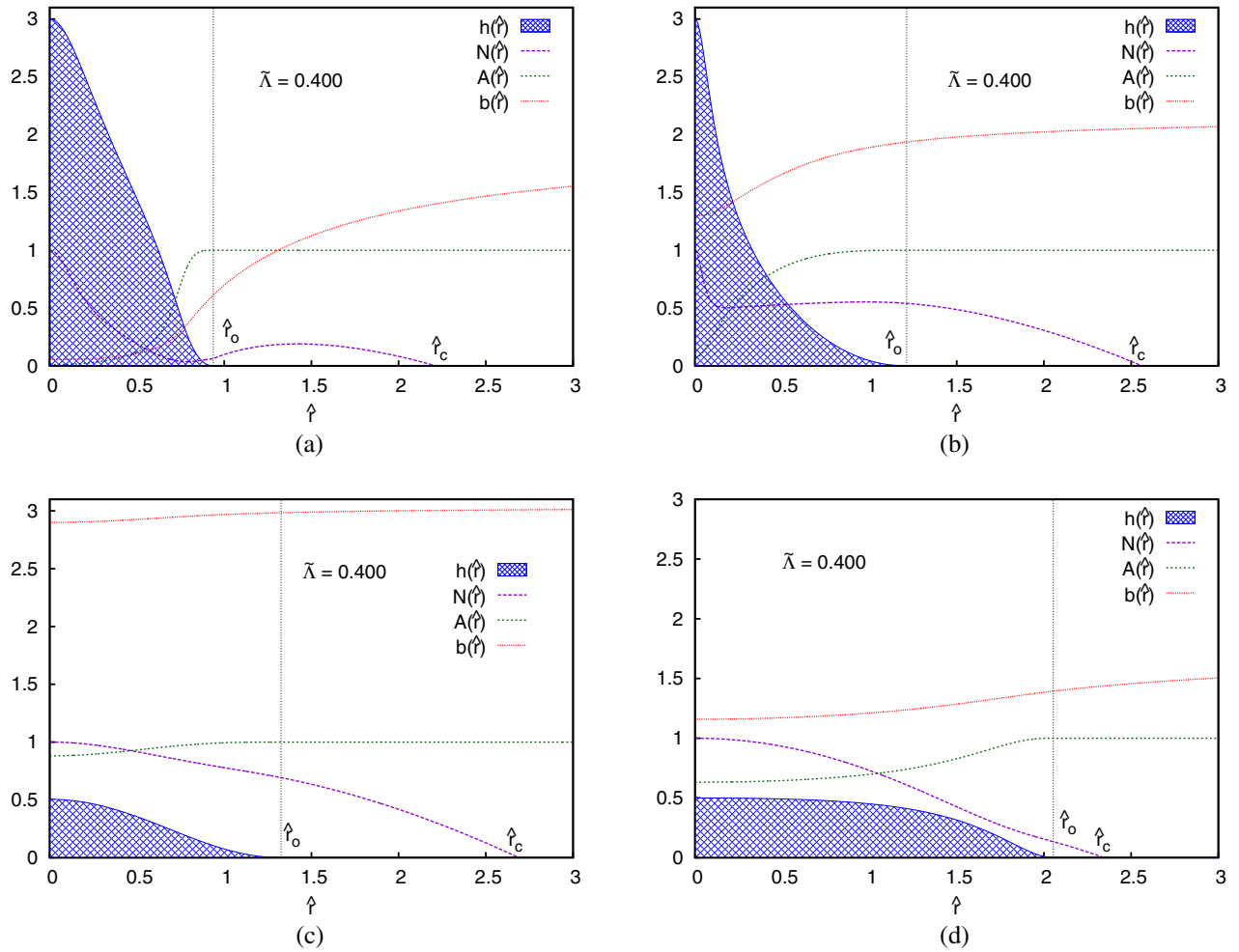

FIG. 8.   Figures (a) to (d) depict plots of $h(\hat{r})$, $N(\hat{r})$, $A(\hat{r})$, and $b(\hat{r})$ vs $\hat{r}$ for $\tilde{\Lambda} = 0.400$ (which corresponds to the dS space).

As we change the value of $\tilde{\Lambda}$ in the dS region from $\tilde{\Lambda} = 0.000$ to $\tilde{\Lambda} = 1.000$, we observe a lot of new rich physics. While going from $\tilde{\Lambda} = 0.000$ to some critical value $\tilde{\Lambda} = \tilde{\Lambda}_{c_1}$, we observe that the solutions exist in two separate domains, IA and IB (as seen in Fig. 1). However, as we increase $\tilde{\Lambda}$

beyond $\tilde{\Lambda} = \tilde{\Lambda}_{c_1}$, the solutions of the theory are seen to exist in regions IIA and IIB (instead of regions IA and IB).

As we increase the value of $\tilde{\Lambda}$ from one critical value $\tilde{\Lambda} = \tilde{\Lambda}_{c_1}$ to another critical value $\tilde{\Lambda} = \tilde{\Lambda}_{c_2}$, we notice that region IIA in the phase diagram shows a continuous
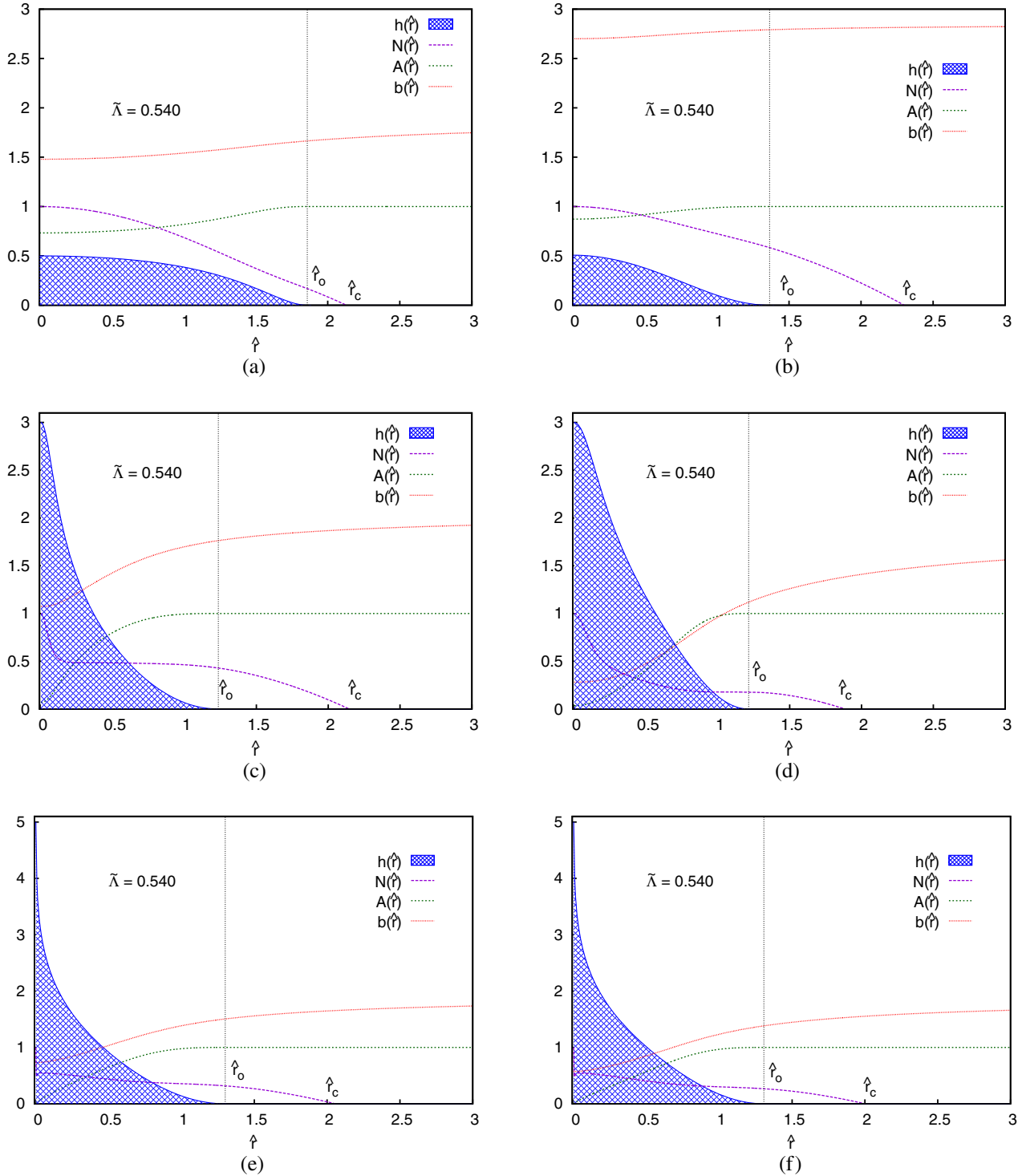

FIG. 9.   Figures (a) to (f) depict plots of $h(\hat{r})$, $N(\hat{r})$, $A(\hat{r})$, and $b(\hat{r})$ vs $\hat{r}$ for $\tilde{\Lambda} = 0.540$ (which corresponds to the dS space).

deformation of the curves, and region IIB is seen to have its own rich physics as explained above.

As we increase $\tilde{\Lambda}$ beyond $\tilde{\Lambda}_{c_2}$, we observe that in region IIA there is again a continuous deformation of the curves all the way up to $\tilde{\Lambda} = 1.000$. The occurrence of more bifurcation points in region IIB and the associated nature of the relevant phase trajectories in the subregions of domain

IIB of the phase diagram of the theory [cf. Figs. 1(a) and 1(b)] has been discussed in details in the foregoing (for many further details of our earlier work, we refer to Ref. [15]).

We wish to emphasize here that a proper understanding of the richness of the physics contents of the theory like the occurrence of multiple bifurcation points in the phase
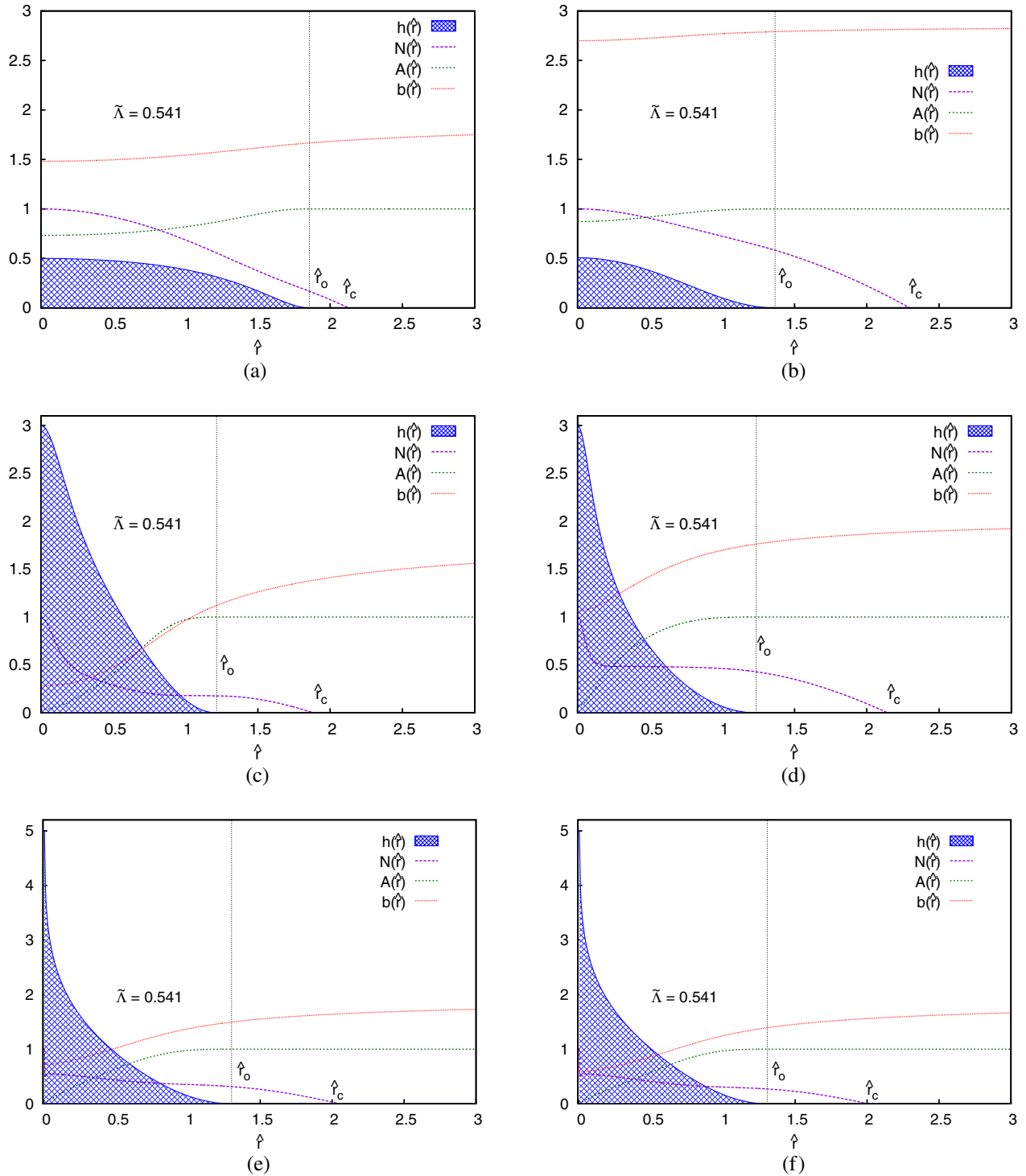

FIG. 10. Figures (a) to (f) depict plots of $h(\hat{r})$, $N(\hat{r})$, $A(\hat{r})$, and $b(\hat{r})$ vs $\hat{r}$ for $\tilde{\Lambda} = 0.541$ (which corresponds to the dS space).

diagram shown in Fig. 1(a) is very crucial for several reasons. This leads not only to a proper understanding of the physics contents of the 2D phase diagrams shown in Figs. 1(b) and 1(c) on the lines parallel to those of Fig. 1(a), but it also leads to a proper understanding of the physics contents of the 3D phase diagrams shown in Figs. 3. This, in fact, has necessitated an appropriate mentioning here of some of the important discussion given in our earlier work (cf. Ref. [15]).

A plot of the vector field at the center of the star $b(0)$ vs the radius $\hat{r}_o$ of the boson star is depicted in Fig. 1(d). As before, the point B_1 corresponds to the bifurcation point, and the entire region depicted in Fig. 1(d) is divided into four regions, IA, IB and IIA, IIB, in the vicinity of the bifurcation point B_1. The asterisks shown in Fig. 1(d) represent the transition points from the boson stars to the boson shells. The spiral behavior of the solutions is visible in regions IA and IIB.

Figures 2(a) and 2(b) represent the *simplified versions* of Figs. 1(a) and 1(b) and depict the phase diagrams of the theory showing respectively the plots of $h(0)$ vs $b(0)$ and

$A(0)$ vs $b(0)$ [where $h(0)$, $b(0)$, and $A(0)$ denote the values of these fields at the center of the star]. Figure 2(c) depicts the phase diagram of the theory involving $N(\hat{r}_o)$ and $b(0)$ [where $N(\hat{r}_o)$ denotes the value of the field at the outer radius of the star]. Figure 2(d) again represents a simplified version of Fig. 1(d) and depicts a plot of $\hat{r}_o$ vs $b(0)$. We wish to emphasize here that Figs. 2 show the plots for eight different values of $\tilde{\Lambda}$ ranging from $\tilde{\Lambda} = -0.020$ to $\tilde{\Lambda} = +1.000$ (covering the AdS as well as dS spaces). It is to be noted here that Figs. 2 are being plotted only for eight different values of $\tilde{\Lambda}$, whereas Figs. 1 are being plotted for 17 different values of $\tilde{\Lambda}$. In this sense, Figs. 2(a), 2(b), and 2(d) represent the simplified versions of Figs. 1(a), 1(b), and 1(d). The figures shown in the insets in Figs. 2(a)–2(d) represent particular sections of these figures with better precision.

We have studied the properties of gravitating boson stars as depicted in Figs. 3(a)–3(f) showing the 3D plots involving the scalar field h and the U(1) gauge field b and the metric field A at the center of the boson star for
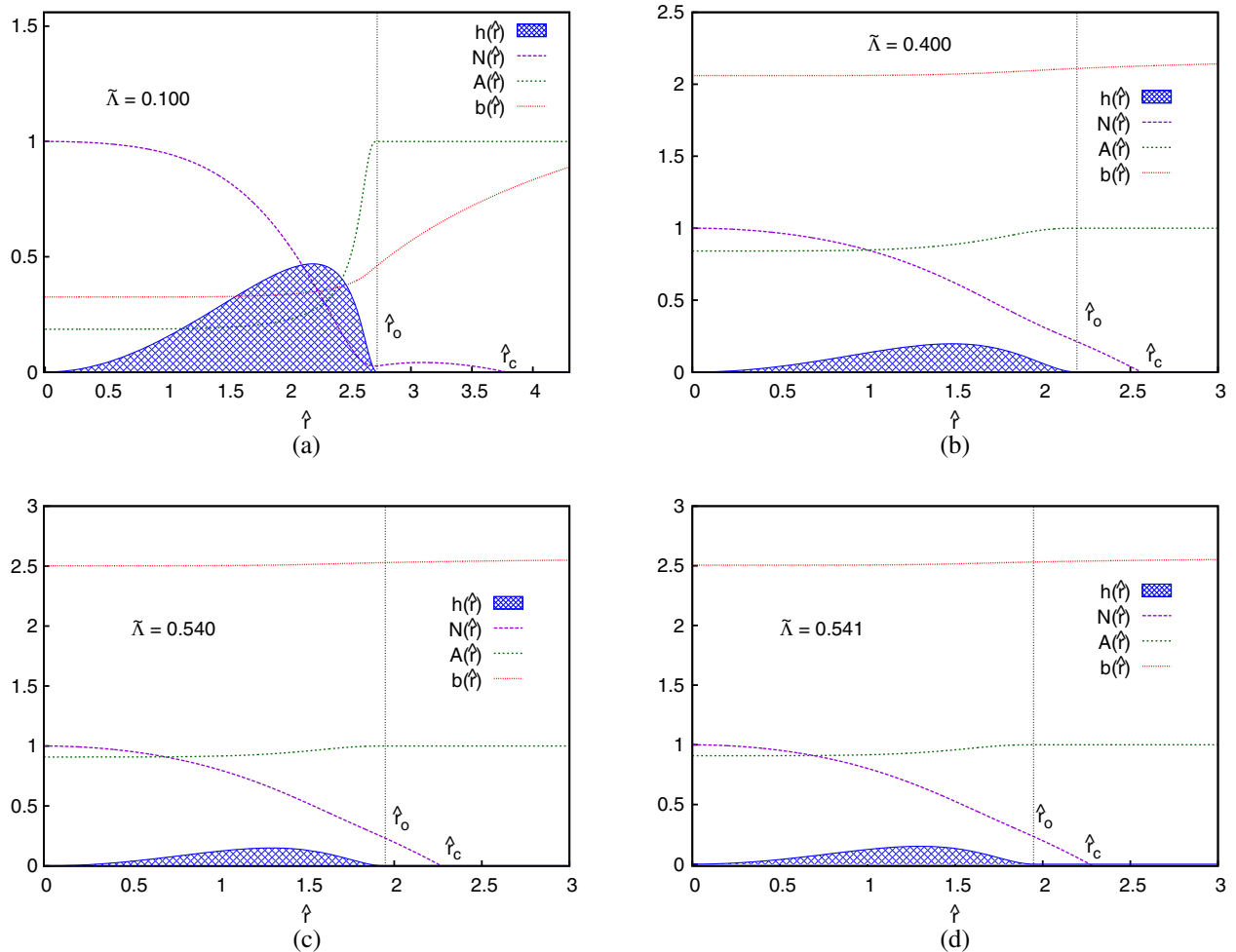

FIG. 11.   Figures (a) to (d) depict plots of $h(\hat{r})$, $N(\hat{r})$, $A(\hat{r})$, and $b(\hat{r})$ vs $\hat{r}$ for shown values of $\tilde{\Lambda}$ (all of which correspond to the dS space). Also, these figures correspond to the transition points of the theory from the bosons stars to the boson shells.

several values of the cosmological constant $\tilde{\Lambda}$ with six different viewing angles. For the viewing angles denoted by (θ, ϕ), we use the convention such that θ denotes the angle of rotation about the ox axis in the counterclockwise direction and can take values between zero and π, and ϕ is the angle of rotation along the oz' axis also in the counterclockwise direction and can take values between zero and 2π. Figures 3(a)–3(f) correspond respectively to the values $(\theta, \phi) \equiv (60, 60)$, $(60, 170)$, $(60, 240)$, $(130, 30)$, $(130, 70)$, and $(130, 350)$.

We have also studied the properties of gravitating boson stars as depicted in Figs. 4(a)–4(f) showing the 3D plot of the scalar field h and the U(1) gauge field b at the center of the boson star and the radius of the star $\hat{r}_o$ for several values of the cosmological constant $\tilde{\Lambda}$ (with six different viewing angles). Figures 4(a)–4(f) correspond respectively to the values $(\theta, \phi) \equiv (60, 100)$, $(112, 17)$, $(60, 200)$, $(35, 245)$, $(140, 60)$, and $(130, 30)$.

In the following, we wish to explain that our 3D plots as depicted in Figs. 3 and 4 with some arbitrary values for (θ, ϕ) could be reduced to the 2D plots as depicted in Fig. 1

by choosing some appropriate values for (θ, ϕ). For example, a choice of $(\theta, \phi) \equiv (0, 0)$ for Figs. 3 and 4 would reduce these 3D plots to the 2D plot shown in Fig. 1(a) with $b(0)$ being plotted on the x axis and $h(0)$ being plotted on the y axis [and $A(0)$ and $\hat{r}_o$ being along the z axis]. Similarly, a choice of $(\theta, \phi) \equiv (90, 0)$ for Figs. 3 and 4 would reduce these 3D plots to the 2D plots shown respectively in Fig. 1(b) [with $b(0)$ being plotted on the x axis and $A(0)$ being plotted on the y axis] and Fig. 1(d) [with $b(0)$ being plotted on the x axis and $\hat{r}_o$ being plotted on the y axis] [and $h(0)$ being along the z axis]. Also, a choice of $(\theta, \phi) \equiv (90, 90)$ for Fig. 3 would reduce the 3D plots of Fig. 3 to the 2D plot shown in Fig. 1(c) with $h(0)$ being plotted on the x axis and $A(0)$ being plotted on the y axis [and $b(0)$ being along the z axis). Also, the asterisks shown in Figs. 3 and 4 corresponding to $h(0) = 0$ represent the transition points from the boson stars to the boson shells.

Further, we have investigated in details the variations of all the four fields involved in our theory, namely $h(\hat{r})$, $N(\hat{r})$, $A(\hat{r})$, and $b(\hat{r})$ with $\hat{r}$ for several values of the cosmological
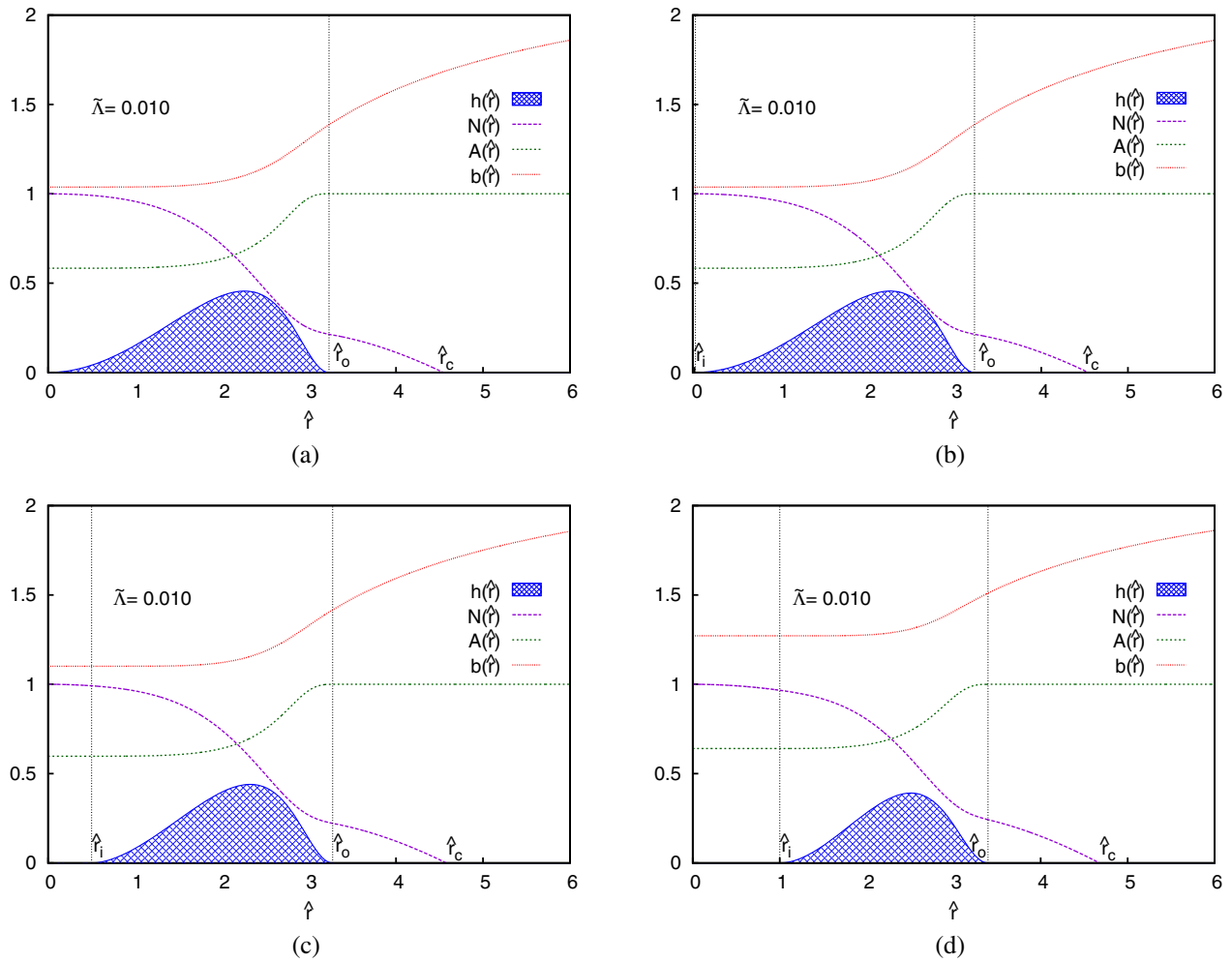

FIG. 12. Figures (a) to (d) depict plots of $h(\hat{r})$, $N(\hat{r})$, $A(\hat{r})$, and $b(\hat{r})$ vs $\hat{r}$ for $\tilde{\Lambda} = 0.010$ (which corresponds to the dS space).

constant $\tilde{\Lambda}$ covering the AdS as well as the dS spaces. The variations of our above investigations are plotted in Figs. 5–13.

Here, Figs. 5(a)–5(d) depict plots of $h(\hat{r})$, $N(\hat{r})$, $A(\hat{r})$, and $b(\hat{r})$ vs $\hat{r}$ for $\tilde{\Lambda} = -0.200$ (which corresponds to the AdS space). In order to understand Figs. 5(a)–5(d) more properly, we consider a hypothetical five-dimensional parameter space spanned by $[\tilde{\Lambda}, N(0), b(0), h(0), A(0)]$. We also remind ourselves that for a study of boson stars we have fixed $N(0) = 1$ for all the cases under study. Next, we pick up cases corresponding to different values of $\tilde{\Lambda}$. In particular, for the case under study represented by Figs. 5(a)–5(d), we choose the case corresponding to $\tilde{\Lambda} = -0.200$ (which corresponds to AdS space). It is to be noted here that this particular curve lies entirely in region IA shown in Figs. 1(a) and 1(b). We then choose a particular value of $b(0)$ [namely $b(0) = 1.735$], and from the phase diagram shown in Fig. 1(a), we pick up four different points (on the curve corresponding to $\tilde{\Lambda} = -0.200$) corresponding to $h(0) = 1.30$, $h(0) = 2.70$,

$h(0) = 3.85$, and $h(0) = 5.65$ for Figs. 5(a)–5(d) respectively. However, we remind ourselves here that, corresponding to these four values of $h(0)$, the corresponding value of $A(0)$ gets automatically fixed by virtue of the solutions of the nonlinear differential equations given by Eqs. (17a)–(17d). We then investigate the variations of the four fields involved in the theory, namely $h(\hat{r})$, $N(\hat{r})$, $A(\hat{r})$, and $b(\hat{r})$ with respect to $\hat{r}$ for the ranges shown in Fig. 5.

This in a way gives us an idea not only about the values of the fields inside as well as outside the boson star but also the variations of these fields in the ranges shown in Fig. 5. In turn, it also explains our motivations behind these studies.

Figures 6(a) and 6(b) depict plots of $h(\hat{r})$, $N(\hat{r})$, $A(\hat{r})$, and $b(\hat{r})$ vs $\hat{r}$ for the case $\tilde{\Lambda} = 0.000$ (which corresponds to the case of the absence of cosmological constant $\tilde{\Lambda}$ in the theory). For Figs. 6(a) and 6(b), we choose two points, $(h(0) = 1.70, \; b(0) = 0.019532)$ and $(h(0) = 1.70, \; b(0) = 1.20812)$, which lie in regions IB and IA respectively in the phase diagram of the theory [cf. Fig. 1(a)] on the curves corresponding to $\tilde{\Lambda} = 0.0$. It
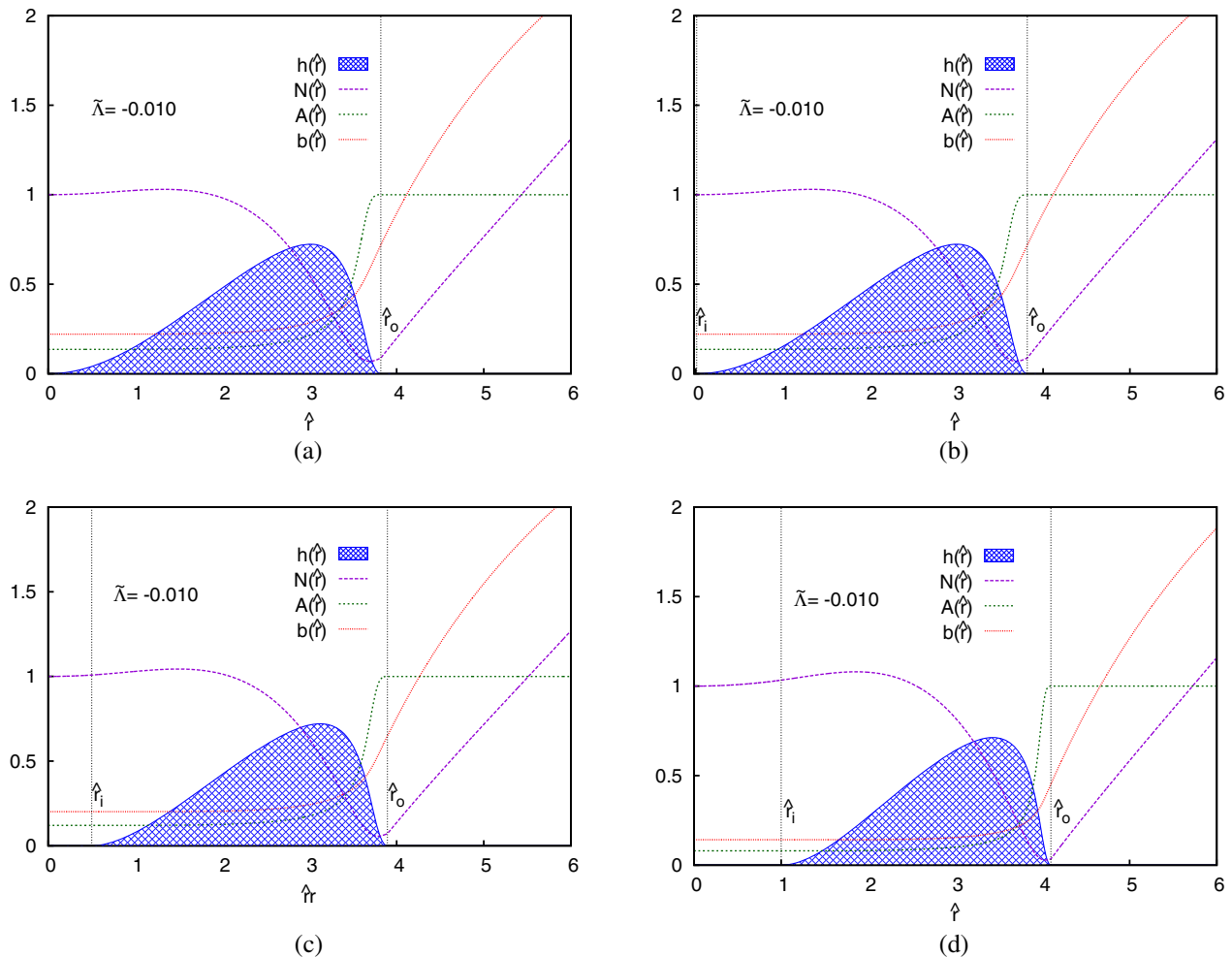

FIG. 13.   Figures (a)–(d) depict plots of $h(\hat{r})$, $N(\hat{r})$, $A(\hat{r})$, and $b(\hat{r})$ vs $\hat{r}$ for $\tilde{\Lambda} = -0.010$ (which corresponds to the AdS space).

is to be noted here that the values of $A(0)$ for these two points get automatically fixed by virtue of the solutions of Eqs. (17a)–(17d). The variations of the four fields involved in the theory, namely $h(\hat{r})$, $N(\hat{r})$, $A(\hat{r})$, and $b(\hat{r})$ are then investigated with respect to $\hat{r}$ for the ranges shown in Figs. 6(a)–6(b).

Figures 7(a)–7(d) depict plots of $h(\hat{r})$, $N(\hat{r})$, $A(\hat{r})$, and $b(\hat{r})$ vs $\hat{r}$ for $\tilde{\Lambda} = 0.100$ (which corresponds to the dS space). For the Figs. 7(a) and 7(b), we choose two points, $(h(0) = 2.00, \quad b(0) = 1.071483)$ and $(h(0) = 2.00, b(0) = 0.07008)$, which lie in regions IB and IA respectively. Also, for Figs. 7(c) and 7(d), we choose another two points, $(h(0) = 2.600, \quad b(0) = 1.450)$ and $(h(0) = 1.24925, \quad b(0) = 1.450)$, both of which lie in region IA of the phase diagram [Fig. 1(a)]. We then study the variations of the four fields involved in the theory, namely $h(\hat{r})$, $N(\hat{r})$, $A(\hat{r})$, and $b(\hat{r})$ vs $\hat{r}$ for the range shown in Figs. 7(a)–7(d). It may be important to emphasize here

that the cases corresponding to the dS space (having positive values of $\tilde{\Lambda}$) would have some definite values for the radius of the cosmological horizon $\hat{r}_c$ as depicted in Figs. 7–12.

Figures 8(a)–8(d) depict plots of $h(\hat{r})$, $N(\hat{r})$, $A(\hat{r})$, and $b(\hat{r})$ vs $\hat{r}$ for $\tilde{\Lambda} = 0.400$ (which corresponds to the dS space). For Figs. 8(a) and 8(b), we choose two points: $(h(0) = 3.0, \quad b(0) = 0.05463)$ and $(h(0) = 3.0, b(0) = 1.29837)$. Both of these points lie in region IIB1 in the phase diagram: Fig. 1(a). Similarly for Figs. 8(c) and 8(d), we choose two points: $(h(0) = 0.50, b(0) = 2.900$ and $h(0) = 0.50, b(0) = 1.15874$. Both of these points lie in region IIA. For these four cases, we then study the variations of the fields of the theory $h(\hat{r})$, $N(\hat{r})$, $A(\hat{r})$, and $b(\hat{r})$ vs $\hat{r}$ for the ranges shown in the figures.

Figures 9(a)–9(f) depict plots of $h(\hat{r})$, $N(\hat{r})$, $A(\hat{r})$, and $b(\hat{r})$ vs $\hat{r}$ for $\tilde{\Lambda} = 0.540$ (which corresponds to the dS space). For Figs. 9(a) and 9(b), we choose two points,
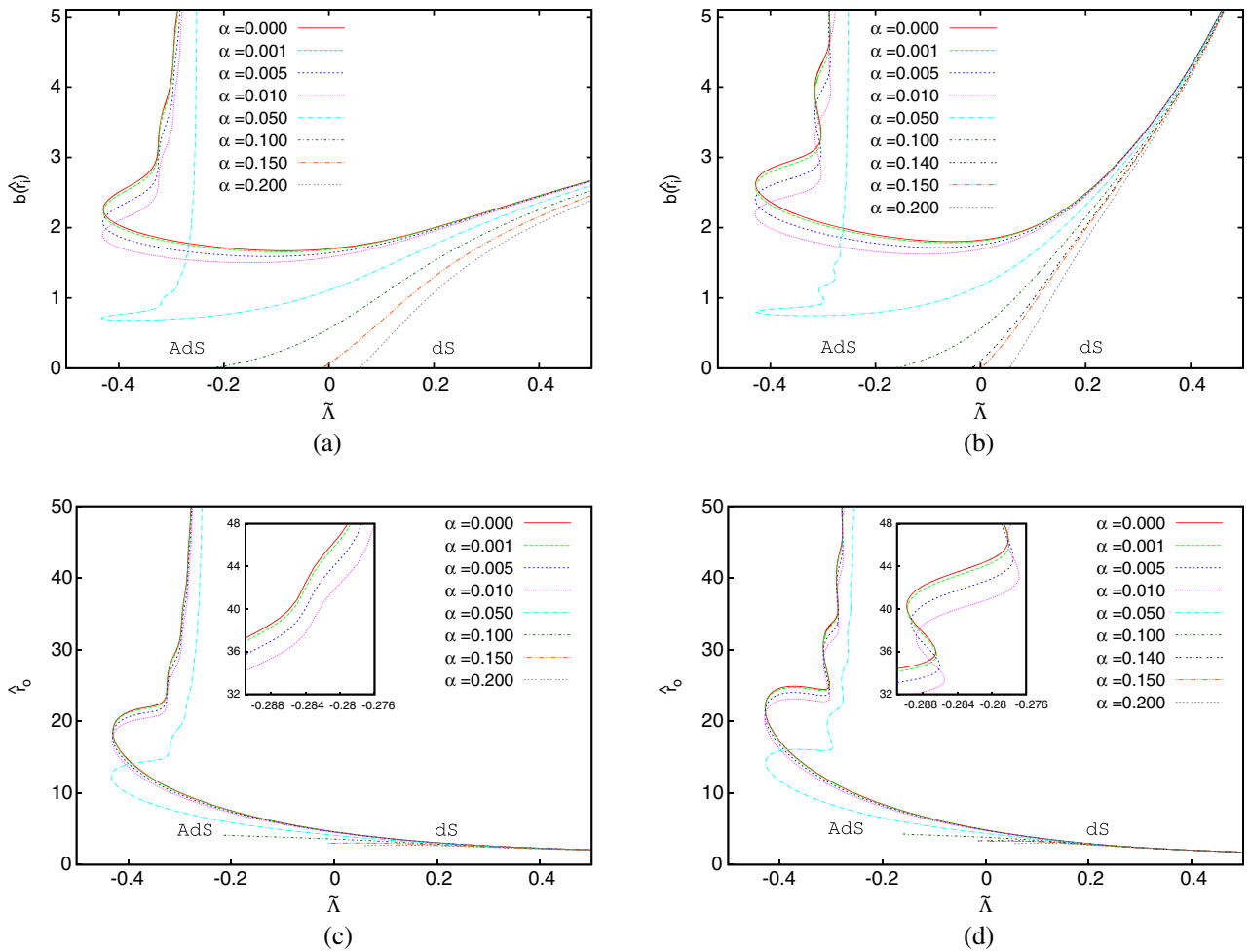

FIG. 14. Figures (a) and (b) show respectively the properties of the gravitating boson stars and boson shells depicting the plot of $b(\hat{r}_i)$ vs $\tilde{\Lambda}$ for several values of α (where $\hat{r}_i = 0$ for the boson stars). Figures (c) and (d) show respectively the properties of the gravitating boson stars and boson shells depicting the plot of $\hat{r}_o$ vs $\tilde{\Lambda}$ for several values of α. The figures in the inset show a part of the plots with a better precision for the depicted range of $\tilde{\Lambda}$.

$(h(0) = 0.50, \quad b(0) = 1.4791)$ and $(h(0) = 0.50, b(0) = 2.700)$, which lie in region IIA in the phase diagram: Fig. 1(a). Similarly for Figs. 9(c) and 9(d), we choose two points, $(h(0) = 3.00, b(0) = 1.0741)$ and $(h(0) = 3.00, b(0) = 0.78123)$, which lie in region IIB2. Again, for Figs. 9(e) and 9(f), we choose two points, $(h(0) = 5.00, \quad b(0) = 0.72877)$ and $(h(0) = 5.00, b(0) = 0.57149)$, which lie in region IIB3a. Corresponding to these six points chosen, we then study the variations of the four fields of the theory $h(\hat{r})$, $N(\hat{r})$, $A(\hat{r})$, and $b(\hat{r})$ vs $\hat{r}$ for the ranges shown in the figures.

Figures 10(a) to 10(f) depict plots of $h(\hat{r})$, $N(\hat{r})$, $A(\hat{r})$, and $b(\hat{r})$ vs $\hat{r}$ for $\tilde{\Lambda} = 0.541$ (which corresponds to the dS space). For Figs. 10(a) and 10(b), we choose two points, $(h(0) = 0.50, b(0) = 1.48133)$ and $(h(0) = 0.50, b(0) = 2.700)$, which lie in region IIA in the phase diagram: Fig. 1(a). Similarly for Figs. 10(c) and 10(d), we choose two

points, $(h(0) = 3.00, b(0) = 0.28354)$ and $(h(0) = 3.00, b(0) = 1.07199)$, which lie in region IIB2. Again for the Figs. 10(e) and 10(f), we choose two points, $(h(0) = 5.00, b(0) = 0.71695)$ and $(h(0) = 5.00, b(0) = 0.58354)$, which lie in region IIB3b. Corresponding to these six points chosen, we then study the variations of the four fields of the theory $h(\hat{r})$, $N(\hat{r})$, $A(\hat{r})$, and $b(\hat{r})$ vs $\hat{r}$ for the ranges shown in the figures. Figures 11(a) to 11(d) depict plots of $h(\hat{r})$, $N(\hat{r})$, $A(\hat{r})$, and $b(\hat{r})$ vs $\hat{r}$ for four values of $\tilde{\Lambda}$, namely $\tilde{\Lambda} = 0.100$, 0.400, 0.540, and 0.541 respectively (all of which correspond to the dS space). Also, these figures correspond to the transition points of the theory from the boson stars to the boson shells, which implies $h(0) = 0.00$ for all four figures. Also, these figures actually correspond to $b(0) = 0.325587$, 2.06006, 2.50273, and 2.50550 respectively. The line $h(0) = 0.00$ in fact, marks one of the boundaries of regions IB and IIA.
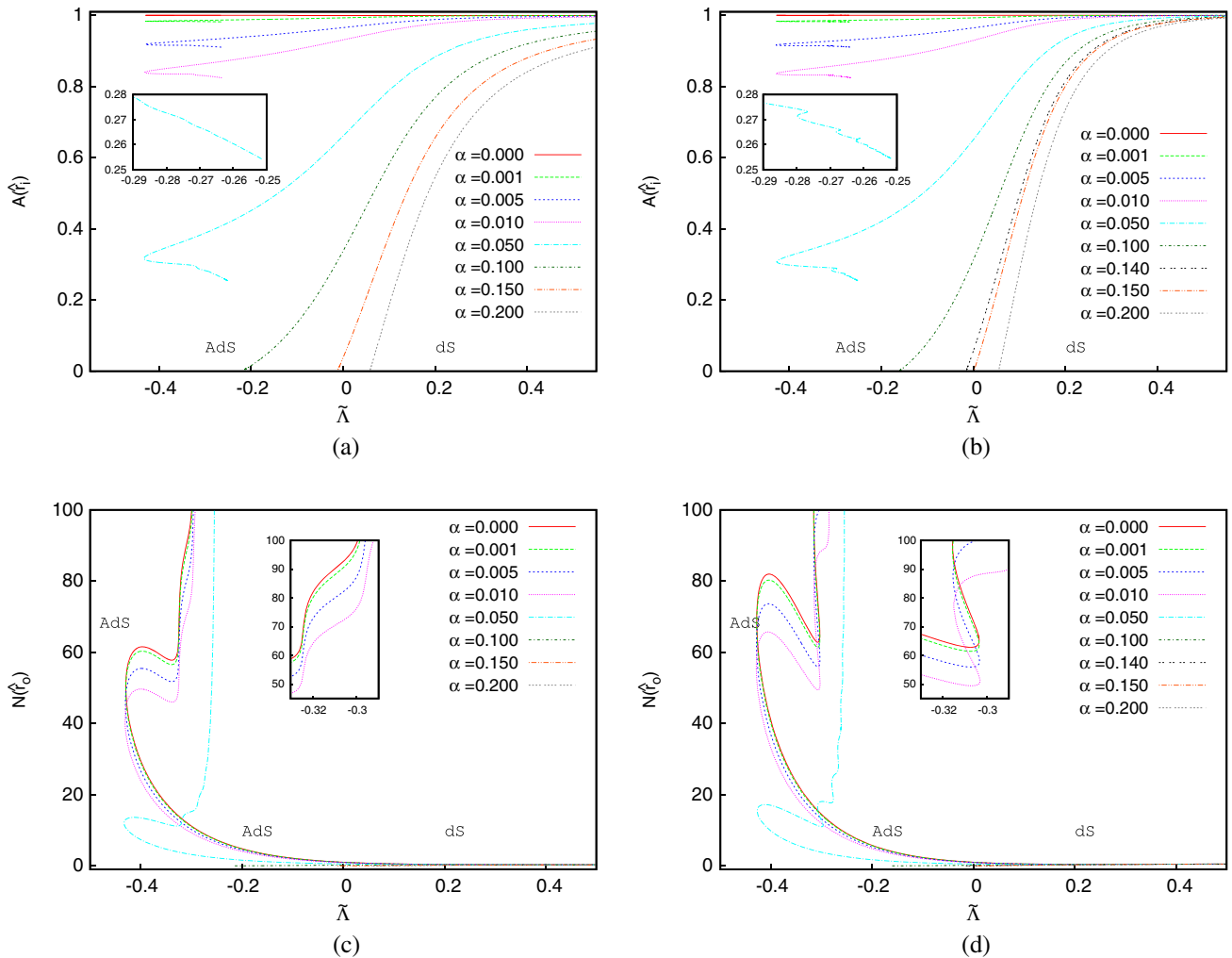

FIG. 15.　Figures (a) and (b) show respectively the properties of the gravitating boson stars and boson shells depicting the plot of $A(\hat{r}_i)$ vs $\tilde{\Lambda}$ for several values of α (where $\hat{r}_i = 0$ for the boson stars). Figures (c) and (d) show respectively the properties of the gravitating boson stars and boson shells depicting the plot of $N(\hat{r}_o)$ vs $\tilde{\Lambda}$ for several values of α. The figures in the inset show a part of the plots with a better precision for the depicted range of $\tilde{\Lambda}$.

Figures 12(a)–12(d) depict plots of $h(\hat{r})$, $N(\hat{r})$, $A(\hat{r})$, and $b(\hat{r})$ vs $\hat{r}$ for the *boson shells* with different values of the inner radius, namely $\hat{r}_i = 0.000, 0.001, 0.500, 1.000$ respectively for $\tilde{\Lambda} = 0.010$ (which corresponds to the dS space).

Figures 13(a)–13(d) depict plots of $h(\hat{r})$, $N(\hat{r})$, $A(\hat{r})$, and $b(\hat{r})$ vs $\hat{r}$ for the boson shells with different values of the inner radius, namely $\hat{r}_i = 0.000, 0.001, 0.500, 1.000$ respectively for $\tilde{\Lambda} = -0.010$ (which corresponds to the AdS space).

We now explain the physics contents of Figs. 14 and 15 and highlight some important points (albeit salient features) of our investigations in the context of these figures. Figures 14 and 15 depict the physical properties of the compact boson star and boson shell solutions where the case $\alpha = 0$ corresponds to the Q-shell solutions. We also determine the domains of existence of these physical properties for some specific values of the parameters of the theory. In our numerical calculations, we have fixed the value of the parameter $\tilde{\lambda}$ to be equal to 1 for the boson stars as well as the boson shells solutions. The value of the parameter $\hat{r}_i$ has been fixed to 1 for the boson shells, and $\hat{r}_i = 0$ for the boson stars.

Figures 14(a) and 14(b) show respectively the properties of the gravitating boson stars and boson shells depicting the plot of $b(\hat{r}_i)$ vs $\tilde{\Lambda}$ for several values of α (where $\hat{r}_i = 0$ for the boson stars), and Figs. 14(c) and 14(d) show respectively the properties of the gravitating boson stars and boson shells depicting the plot of $\hat{r}_o$ vs $\tilde{\Lambda}$ for several values of α. The figures in the insets show a part of these plots with a better precision for the depicted range of $\tilde{\Lambda}$.

It is apparent from these figures that the minimum value of $b(\hat{r}_i)$ for a particular value of $\tilde{\Lambda}$ keeps decreasing with the increasing value of α until the value of $b(\hat{r}_i)$ reaches zero. In fact, the plot for a particular value of α continuously deforms itself as we increase the value of α. This scenario is more transparent in the domain where the cosmological constant $\tilde{\Lambda}$ is negative (i.e. in the AdS space). Actually, with the increase in the value of α, the solutions cease to exist in the AdS region for $\alpha \geq 0.150$. For $\alpha \geq 0.150$, the solutions do continue to exist, however, only in the dS region. Also within the AdS region, the damped oscillations of the cosmological constant $\tilde{\Lambda}$ with increasing $b(\hat{r}_i)$ are seen in Figs. 14(a) and 14(b) for some smaller values of α.

Figures 15(a) and 15(b) show respectively the properties of the gravitating boson stars and boson shells depicting the plot of $A(\hat{r}_i)$ vs $\tilde{\Lambda}$ for several values of α (where $\hat{r}_i = 0$ for the boson stars), and Figs. 15(c) and 15(d) show respectively the properties of the gravitating boson stars and boson shells depicting the plot of $N(\hat{r}_o)$ vs $\tilde{\Lambda}$ for several values of α. Figures in the insets show a part of these plots with better precision for the depicted range of $\tilde{\Lambda}$.

It is apparent from these figures that there is a continuous deformation of the curves as we increase or decrease the value of the cosmological constant $\tilde{\Lambda}$.

VI. SUMMARY AND CONCLUSIONS

The boson stars and boson shells representing the localized self-gravitating solutions have been studied in the literature in the presence of positive as well as negative values of the cosmological constant Λ. The theories in the dS space (corresponding to positive values of Λ) describe a somewhat realistic description of the compact stars and are relevant from observational point of view. They are also used in the dark energy models of the Universe. However, the theories in the AdS space (with negative values of Λ) are important for the AdS/CFT theories.

In our earlier work (cf. Ref. [16]), we studied the boson stars and boson shells in a theory of complex scalar field coupled to the $U(1)$ gauge field A_μ and the gravity in the presence of a positive cosmological constant (i.e. in the dS space). However, in the present work, we have studied this theory in the presence of positive as well as negative values of the cosmological constant treated as a free parameter. This allows us to study the theory in the dS as well as in the AdS space. Also, in Ref. [15], we have studied the boson stars in a theory of complex scalar field coupled to the $U(1)$ gauge field A_μ and the gravity in the presence of a positive as well as negative cosmological constant, whereas in the present work, we have studied not only the boson stars but also the boson shells in this theory.

As in Ref. [15], in our present work also, we have studied the theory in the presence of a potential: $V(|\Phi|) := (m^2|\Phi|^2 + \lambda|\Phi|)$ (with m and λ being constant parameters). We have investigated properties of the solutions of this theory and determined their domains of existence for some specific values of the parameters of the theory.

It is important to emphasize here as also explained in the Introduction that similar solutions have also been obtained by Kleihaus *et al.* in a theory involving massless complex scalar fields coupled to the U(1) gauge field and gravity in a conical potential in the absence of a cosmological constant Λ [10,11]. They have obtained explicitly the domain of the existence of compact boson stars and boson shells. They have also considered the boson shells, which do not have an empty inner region $r < r_i$, but instead they harbor a Schwarzschild black hole or a Reissner-Nordström black hole in the region $r < r_i$ [10,11].

As mentioned in the foregoing, polynomial potentials have also been used in the literature for a study of the boson stars. For a study of the *compact* boson stars, presence of the *conical piece* of the potential is very crucial. However, the choice of the massless scalar fields (instead of the massive scalar fields as considered in the present work) in the theory reduces the number of free parameters of the theory by one and is expected to produce the results

conceptually somewhat similar to our present results although with different numerical details (albeit, with different domains of existence). These studies are currently underway and will be reported later. The inclusion of the quartic and/or sextic terms in the potential is expected to bring in some new additional features in the results. We propose to undertake such studies in the near future.

In the present work, we have constructed the boson star and boson shell solutions of this theory numerically, and we have studied their properties by assuming the interior of the shells to be empty space (dS like or AdS like).

In this work, we have shown that these charged shell-like solutions persist in the presence of not only the positive cosmological constant (corresponding to dS space) but also for the negative cosmological constant (corresponding to AdS space).

The self-gravitating compact boson shells constructed in our present work possess an empty dS-like or AdS-like interior region, $\hat{r} < \hat{r}_i$, and a Reissner-Nordström-dS or Reissner-Nordström-AdS exterior region, $\hat{r} > \hat{r}_o$.

In our future work, we also propose considering the possibility of the filling of the interior region of the boson shells with black holes, analogous to the study in Ref. [11]. It would also be interesting to extend our present studies of the charged compact boson star and boson shell solutions to other dimensions.

[1] D. A. Feinblum and W. A. McKinley, Phys. Rev. **168**, 1445 (1968).
[2] D. J. Kaup, Phys. Rev. **172**, 1331 (1968).
[3] R. Ruffini and S. Bonazzola, Phys. Rev. **187**, 1767 (1969).
[4] P. Jetzer, Phys. Rep. **220**, 163 (1992).
[5] T. Lee and Y. Pang, Phys. Rep. **221**, 251 (1992).
[6] E. W. Mielke and F. E. Schunck, Nucl. Phys. **B564**, 185 (2000).
[7] S. L. Liebling and C. Palenzuela, Living Rev. Relativ. **15**, 6 (2012).
[8] R. Friedberg, T. Lee, and A. Sirlin, Phys. Rev. D **13**, 2739 (1976).
[9] S. R. Coleman, Nucl. Phys. **B262**, 263 (1985).
[10] B. Kleihaus, J. Kunz, C. Lammerzahl, and M. List, Phys. Lett. B **675**, 102 (2009).
[11] B. Kleihaus, J. Kunz, C. Lammerzahl, and M. List, Phys. Rev. D **82**, 104050 (2010).
[12] B. Hartmann, B. Kleihaus, J. Kunz, and I. Schaffer, Phys. Lett. B **714**, 120 (2012).
[13] B. Hartmann and J. Riedel, Phys. Rev. D **86**, 104008 (2012).
[14] B. Hartmann, B. Kleihaus, J. Kunz, and I. Schaffer, Phys. Rev. D **88**, 124033 (2013).
[15] S. Kumar, U. Kulshreshtha, and D. S. Kulshreshtha, Phys. Rev. D **93**, 101501 (2016).
[16] S. Kumar, U. Kulshreshtha, and D. Shankar Kulshreshtha, Classical Quantum Gravity **31**, 167001 (2014).

[17] S. Kumar, U. Kulshreshtha, and D. S. Kulshreshtha, Gen. Relativ. Gravit. **47**, 76 (2015).
[18] D. Astefanesei and E. Radu, Nucl. Phys. **B665**, 594 (2003).
[19] E. Radu and B. Subagyo, Phys. Lett. B **717**, 450 (2012).
[20] A. Prikas, Gen. Relativ. Gravit. **36**, 1841 (2004).
[21] Y. Brihaye, B. Hartmann, and S. Tojiev, Classical Quantum Gravity **30**, 115009 (2013).
[22] D. Pugliese, H. Quevedo, Jorge A. Rueda H., and R. Ruffini, Phys. Rev. D **88**, 024053 (2013).
[23] Y. Brihaye, V. Diemer, and B. Hartmann, Phys. Rev. D **89**, 084048 (2014).
[24] O. Kichakova, J. Kunz, and E. Radu, Phys. Lett. B **728**, 328 (2014).
[25] V. Dzhunushaliev, V. Folomeev, C. Hoffmann, B. Kleihaus, and J. Kunz, Phys. Rev. D **90**, 124038 (2014).
[26] H. Arodz and J. Lis, Phys. Rev. D **77**, 107702 (2008).
[27] H. Arodz and J. Lis, Phys. Rev. D **79**, 045002 (2009).
[28] H. Arodz, J. Karkowski, and Z. Swierczynski, Acta Phys. Polon. B **43**, 79 (2012).
[29] J. M. Maldacena, Int. J. Theor. Phys. **38**, 1113 (1999); Adv. Theor. Math. Phys. **2**, 231 (1998).
[30] E. Witten, Adv. Theor. Math. Phys. **2**, 253 (1998).
[31] S. J. Brodsky, F.-G. Cao, and G. F. de Teramond, Commun. Theor. Phys. **57**, 641 (2012).